

Article

# Effects of Burst Ratio and Frequency on the Passage Vortex Reduction of a Linear Turbine Cascade Using a Dielectric Barrier Discharge Plasma Actuator

Takayuki Matsunuma 

National Institute of Advanced Industrial Science and Technology (AIST), 1-2-1 Namiki, Tsukuba 305-8564, Japan; t-matsunuma@aist.go.jp

**Abstract:** A dielectric barrier discharge plasma actuator was employed to reduce the passage vortex generated in a turbine cascade. This study focused on the burst mode drive of a plasma actuator and examined the relationship between flow field changes and the burst ratio and frequency. The non-dimensionalized burst frequency was fixed at  $F^+ = 1.26$ , and the burst ratio was varied from 0.01 (1% operation) to 1 (100% operation, continuous mode). Generally, an increase in the burst ratio weakens the passage vortex, and the center of the passage vortex moves more toward the upper endwall surface and blade suction surface side. However, the velocity distribution, secondary flow streamlines, turbulence intensity distribution, and vorticity distribution did not change proportionally with changes in the burst ratio. Furthermore, the burst ratio was fixed at  $BR = 0.5$ , and the non-dimensional burst frequency varied from  $F^+ = 0.013$  to 62.9. Low burst frequencies led to a decrease in the peak velocity of the passage vortex, vorticity at the passage vortex center, and negative peak vorticity; however, an increase in the distance of the center of the passage vortex from the upper endwall surface and the turbulence intensity at the vortex center was observed. In contrast, high burst frequencies resulted in a decrease in the position of the vortex center and the turbulence intensity of the passage vortex center, while the peak velocity of the passage vortex, vorticity at the vortex center, and negative peak vorticity increased. The non-dimensionalized burst frequency around  $F^+ = 1$  is appropriate because both effects are balanced.

**Keywords:** plasma actuator; burst mode operation; turbine blade; secondary flow; passage vortex; active flow control; particle image velocimetry



**Citation:** Matsunuma, T. Effects of Burst Ratio and Frequency on the Passage Vortex Reduction of a Linear Turbine Cascade Using a Dielectric Barrier Discharge Plasma Actuator. *Actuators* **2022**, *11*, 210. <https://doi.org/10.3390/act11080210>

Academic Editor: Kenji Uchino

Received: 30 May 2022

Accepted: 28 July 2022

Published: 29 July 2022

**Publisher's Note:** MDPI stays neutral with regard to jurisdictional claims in published maps and institutional affiliations.



**Copyright:** © 2022 by the author. Licensee MDPI, Basel, Switzerland. This article is an open access article distributed under the terms and conditions of the Creative Commons Attribution (CC BY) license (<https://creativecommons.org/licenses/by/4.0/>).

## 1. Introduction

Dielectric barrier discharge (DBD) plasma actuators are attracting attention as active flow control devices. Their features include a simple structure without mechanical moving parts; this offers flexibility of installation and high response speed owing to the electrical control. Figure 1 shows a plasma actuator consisting of two electrodes separated by a dielectric material. In general, the two electrodes are arranged asymmetrically and slightly overlapped, with one electrode exposed to air and the other embedded in the dielectric material. Plasma is generated at the end of the surface electrode by applying a high voltage (ranging approximately between 1 kV<sub>p-p</sub> and 60 kV<sub>p-p</sub>) at a high frequency of several kHz between the electrodes of the plasma actuator. This plasma (ionized air) can exert a body force on the surrounding air via the gradient of the electric field, which induces a one-way flow along the surface. Comprehensive reviews of DBD plasma actuators are presented by Corke et al. [1,2] and Wang et al. [3].

In this study, a high-voltage power amplifier drives the plasma actuator by inputting a signal from a function generator, which, when adjusted, operates the actuator under various waveform conditions.

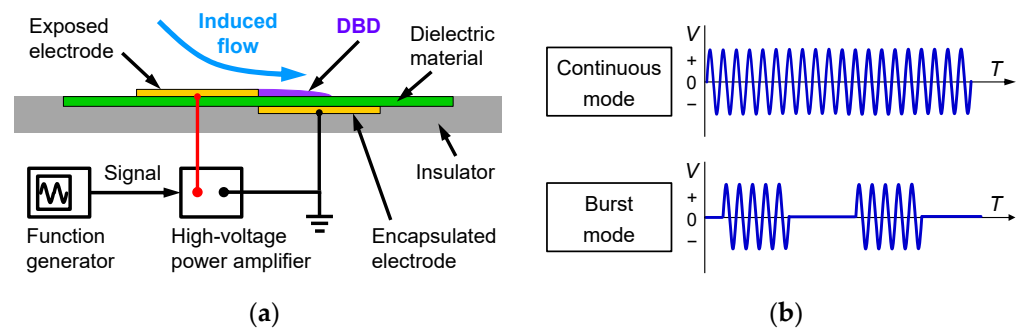


**Figure 1.** DBD plasma actuator: (a) schematic diagram; (b) different operation modes (continuous and burst modes).

Plasma actuators are operated under two driving methods: continuous (steady drive) and burst (unsteady drive) modes of operation. The voltage waveforms of the continuous and burst modes are shown in Figure 1b.

Several studies have been conducted on the effect of burst mode operation of plasma actuators, mainly on the control of flow separation on the suction surface side of a single airfoil [4–12]. The flow separation reduction effect is higher in burst mode control than that in continuous mode control; the intermittent drive of burst mode operation requires less power consumption than continuous mode operation. Generally, the control effect in burst mode reaches its maximum as the non-dimensionalized burst frequency  $F^+$  (corresponding to the Strouhal number) reaches approximately unity. In contrast, Sato et al. [11] used computational fluid dynamics (CFD) to investigate the effect of burst mode control of a NACA0015 airfoil over a wide range of Reynolds numbers in the order of  $10^3$ – $10^6$ . They showed that  $F^+ = 1$  becomes the optimal value at some Reynolds numbers ( $Re = 1.0 \times 10^4$  and  $1.6 \times 10^6$ ) owing to the flow separation reduction effect and that  $F^+ = 10$  becomes the optimal value at some Reynolds numbers ( $Re = 6.3 \times 10^4$  and  $2.6 \times 10^5$ ) owing to the turbulence promotion effect of the boundary layer.

In other studies not involving single airfoils, Koide et al. [13], Li et al. [14], and Saddoughi et al. [15] applied burst drive control to suppress the separation flow after a backward-facing step, suppress the corner separation flow of the compressor cascade, and improve the surge margin of a transonic compressor, respectively.

In turbine blades, plasma actuators provide flow separation reduction on the blade suction surface [16–19]. Huang et al. [16] experimentally studied the effect of burst mode operation on flow separation control at the suction surface side of a low-pressure turbine cascade. Their study revealed that a 10% burst mode drive provided the same separation reduction effect as a continuous mode drive, resulting in more efficiency for power consumption. In addition, Rizzetta and Visbal [17] compared the continuous mode drive and burst mode drives (50%) using CFD and showed that the burst mode drive had a higher flow separation reduction effect.

In contrast, there have only been a few studies on secondary flow control in turbomachinery using plasma actuators. Two important secondary flows occur in turbine blades [20]: tip leakage and passage vortices. Stephens et al. [21], Van Ness II et al. [22], Wang et al. [23], and Yu et al. [24–26] conducted studies using plasma actuators to suppress the tip leakage vortex, formed by the flow leaking from the pressure surface side to the suction surface side through the tip gap of the turbine rotor blade. All of these studies used the continuous mode drive of plasma actuators. Furthermore, a study was conducted to suppress passage vortices using a plasma actuator [27]. Figure 2 presents an overview of the passage vortex generated in the turbine blade row. The passage vortex is a vortex in which the boundary layer upstream of the turbine collides with the leading edge of the turbine blade. The inlet boundary layer rolls up to form a horseshoe vortex, which moves to the suction surface side of the adjacent blade; the vortex further develops while adding the endwall boundary layer inside the blade row. All studies applying these plasma actuators to the suppression of secondary flow in the turbine blade row have used continuous mode

drive control, and, so far, no study has been published using a plasma actuator in burst mode drive for secondary flow control.

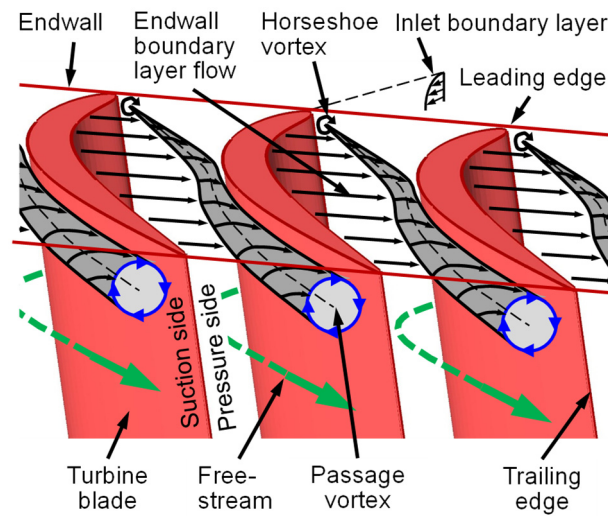


**Figure 2.** Passage vortex generated in turbine blades.

This is a continuation of my previous work on the use of plasma actuators that reduce the passage vortex of a linear turbine cascade [27]. This study aims to examine the effects of the burst mode operation of plasma actuators.

## 2. Experimental Method

### 2.1. Wind Tunnel and Linear Turbine Cascade

Figure 3 shows the measurement section of the linear turbine cascade. As shown in Figure 3a, the airflow coming from the blower of the small blowing-type wind tunnel was sent through a contraction nozzle to the measurement section, where a linear turbine cascade with six blades was installed. The secondary flow velocity distributions downstream of the turbine cascade were measured using two-dimensional particle image velocimetry (PIV) with a measurement area of 56.1 mm × 44.5 mm. It should be noted that the measured velocity did not include the mainstream velocity component (velocity component perpendicular to the PIV measurement plane) because of two velocity component measurements.

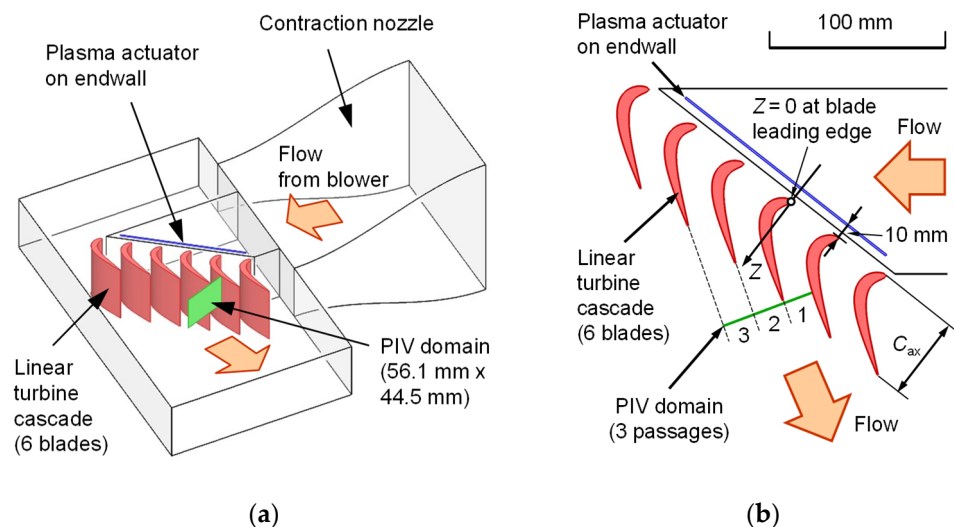


**Figure 3.** Test section of the linear turbine cascade: (a) overall view; (b) top view and blade geometry.

Figure 3b shows the tip view and blade geometry of the measurement section. The plasma actuator was installed 10 mm upstream of the leading edge of the cascade. This was

located 20% upstream of the axial blade chord length using a non-dimensionalized blade axial chord length ( $Z/C_{ax} = -0.20$ ), which is an optimal installation position, as established in a previous study [27]. The measurement range of PIV, indicated by the green line, was located exactly between the three blade passages.

Table 1 lists the specifications of the linear turbine cascade. The blade was shaped based on the blade hub section of the annular turbine cascade [28].

**Table 1.** Specifications of the linear turbine cascade.

Parameter	Symbol	Value
Number of blades	$N$	6
Chord length	$C$	58.65 mm
Axial chord length	$C_{ax}$	49.43 mm
Blade height	$H$	75.00 mm
Blade pitch	$S$	35.47 mm
Inlet flow angle	$\alpha_1$	$51.86^\circ$
Outlet flow angle	$\alpha_2$	$58.74^\circ$
Turning angle	$\alpha_1 + \alpha_2$	$110.60^\circ$
Stagger angle	$\zeta$	$33.43^\circ$

The rotational velocity of the wind tunnel blower was maintained at a constant value of 225 Hz, where the inlet and outlet velocities of the linear turbine cascade were 3.9 and 4.7 m/s and the Reynolds number based on the outlet freestream velocity and blade chord length of the linear turbine cascade was  $1.8 \times 10^4$ . The inlet and outlet velocities were sufficiently stable when the rotating speed of the blower was maintained constant.

## 2.2. PIV Measurements and Data Processing

PIV was employed to quantify the two-dimensional velocity fields at the outlet of the linear turbine cascade using a 15 mJ/pulse, double-pulsed Nd-YAG laser (NANO S30-15PIV, Litron Laser Ltd., Rugby, Warwickshire, United Kingdom). Atomized dioctyl sebacate (DOS) oil with a mean particle diameter of  $1 \mu\text{m}$  was injected upstream of the blower of the wind tunnel via a pressurized oil chamber (LSG-500, Kanomax Japan Inc., Suita, Osaka, Japan). Flow image pairs were captured using a camera (PIV CAM 13-8, TSI Inc., Shoreview, Minnesota, USA) with a resolution of  $1280 \times 1024$  pixels and a frame rate of 3.75 Hz. PIV software (Insight Ver. 3.53, TSI Inc., Shoreview, MN, USA) was used to calculate the velocity vectors from the peak correlation of groups of particles between frames using conventional cross-correlation algorithms on a  $32 \times 32$  pixel grid. Three hundred instantaneous velocity pairs obtained via PIV were used to analyze the time-averaged velocity distributions. From a preliminary experiment, 200 instantaneous velocity pairs or more were sufficient for data averaging. The number of PIV image pairs (300 pairs) was limited by the capacity of the random access memory (RAM) of the computer used. The image pairs were measured in 80 s ( $=300 \text{ pairs}/3.75 \text{ Hz}$ ), and the storage time from RAM to a hard disk was approximately 90 s. Therefore, the PIV measurement time per parameter was approximately 3 min.

Average velocity,  $U_{XY}$ , was calculated as follows:

$$U_{XY} = \left( \sqrt{U_X^2 + U_Y^2} \right) / U_{FS,out} \quad (1)$$

where  $U_X$  and  $U_Y$  are the horizontal and vertical velocity components.

Turbulence intensity,  $Tu_{XY}$ , was also calculated as follows:

$$Tu_{XY} (\%) = 100 \times \left( \sqrt{\frac{u_X'^2 + u_Y'^2}{2}} \right) / U_{FS,out} \quad (2)$$

where  $u_X'$  and  $u_Y'$  are the random velocity fluctuation components in the X and Y directions, respectively.

The velocity and turbulence intensity were non-dimensionalized by a 4.7 m/s freestream velocity at the turbine outlet,  $U_{FS,out}$ .

The vorticity component,  $\Omega_{XY}$ , was calculated as follows:

$$\Omega_{XY} \text{ (1/s)} = \frac{\partial U_Y}{\partial X} - \frac{\partial U_X}{\partial Y} \quad (3)$$

### 2.3. Plasma Actuator

Figure 4 shows a photograph and the cross-sectional structure of the plasma actuator, which was created by a printed circuit board (PCB) process [27]. The exposed top and encapsulated bottom electrodes were designed using computer-aided design software (AutoCAD LT 2014, Autodesk Inc., San Rafael, CA, USA) and were formed by etching a double-sided copper-clad laminate with a dielectric barrier layer made of silicone resin (CS-3975A, Risho Kogyo Co., Ltd., Osaka, Japan). The thicknesses of the copper exposed and encapsulated electrodes and the silicone resin dielectric barrier were 0.018 mm and 0.44 mm, respectively. The span-wise width of electrodes was designed to be 150 mm, while the streamwise lengths of the exposed and encapsulated electrodes were 5 mm and 15 mm, respectively. As shown in Figure 4, the electrodes were arranged asymmetrically in the streamwise direction and overlapped by 0.5 mm in order to generate uniform DBD plasma near one edge of the side of the exposed electrode.

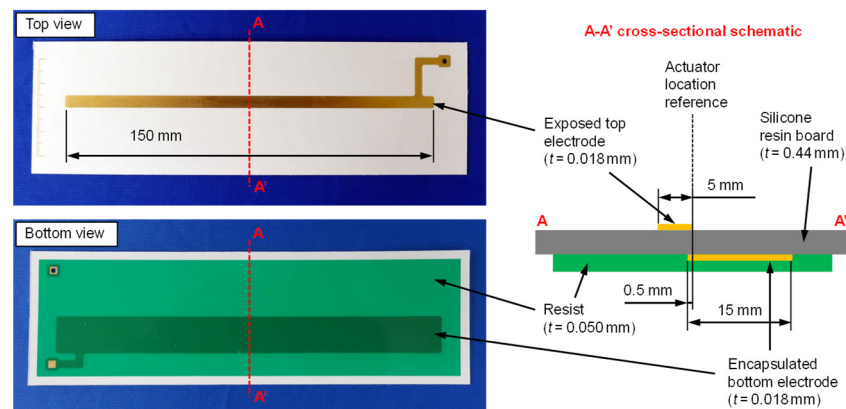


**Figure 4.** Photographs of the top and bottom views (left) and cross-sectional schematic (right) of the DBD plasma actuator.

Plasma actuators were driven by a high-voltage power amplifier (HAPS-10B40, Matsusada Precision, Inc., Kusatsu, Shiga, Japan). Inputting the arbitrary waveform produced by a multifunction generator (WF1974, NF Corp., Yokohama, Kanagawa, Japan) amplifies the input signal a thousandfold. In this experiment, the shape of the excitation waveform was sinusoidal. The amplitude of the peak-to-peak input voltage of the plasma actuator was fixed at 12 kV<sub>p-p</sub>, and the input voltage frequency was fixed at 10 kHz. Regarding the durability of the plasma actuator used, the limitation of the input voltage was approximately 15 kV<sub>p-p</sub>. When applying 15 kV<sub>p-p</sub>, the plasma actuator broke occasionally. However, under the input voltage of 14 kV<sub>p-p</sub>, the plasma actuator showed no instances of breaking at a total accumulated operating time of over 8 h. In the case of continuous mode operation, the maximum absolute velocity induced by the plasma actuator was 3.8 m/s, and the power consumption per plasma actuator unit length (1 m) in continuous mode operation was 166 W/m. The power consumption was measured by the voltage–charge (V-Q) Lissajous method [29,30]. In the case of burst mode operation, the power consumption was proportional to the burst ratio (defined in Section 2.4.2) [31].

2.4. Burst Mode Operation Conditions

2.4.1. Burst Waveform

Figure 5 shows a diagram of the burst waveform. One sine wave (red line) becomes the base sine wave, and one burst wave (blue line) contains the incorporated continuous operation sine waves ( $T_{on}$ ) and non-operation time ( $T_{off}$ ).

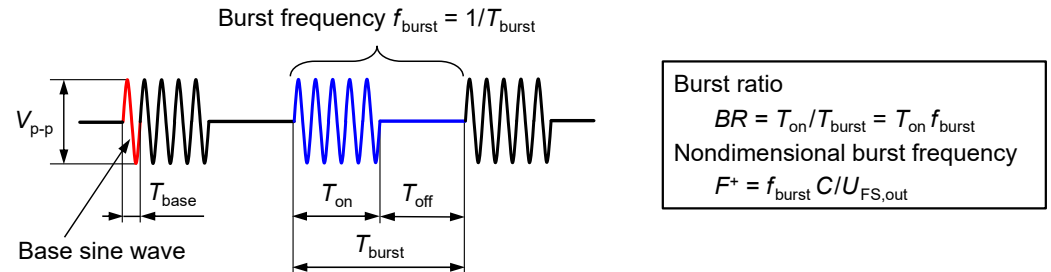


Figure 5. Diagram of burst waveform.

The burst frequency is defined as follows:

$$f_{burst} = \frac{1}{T_{burst}} \tag{4}$$

2.4.2. Burst Ratio

Table 2 lists the various burst ratios for each burst mode experiment. The input voltage of the plasma actuator was fixed at  $V_{p-p} = 12$  kV. The base frequency, burst frequency, and non-dimensionalized frequency were fixed at  $f_{base} = 10,000$  Hz,  $f_{burst} = 100$  Hz, and  $F^+ = 1.26$ , respectively (the definition of  $F^+$  is described in Section 2.4.3). The burst ratio  $BR$  is defined as follows:

$$BR = \frac{T_{on}}{T_{burst}} = T_{on} \times f_{burst} \tag{5}$$

Table 2. Burst mode operation at various burst ratios at fixed  $V_{p-p} = 12$  kV,  $f_{base} = 10,000$  Hz,  $f_{burst} = 100$  Hz, and  $F^+ = 1.26$ .

Burst Ratio, $BR$	Operation Number of Sine Waves at One Burst Cycle	Non-Operation Number of Sine Waves at One Burst Cycle	Operation Time at One Burst Cycle, $T_{on}$ (ms)	Non-Operation Time at One Burst Cycle, $T_{off}$ (ms)
0.01	1	99	0.1	9.9
0.02	2	98	0.2	9.8
0.05	5	95	0.5	9.5
0.1	10	90	1	9
0.2	20	80	2	8
0.3	30	70	3	7
0.4	40	60	4	6
0.5	50	50	5	5
0.6	60	40	6	4
0.7	70	30	7	3
0.8	80	20	8	2
0.9	90	10	9	1
1 (continuance)	100	0	—	—

The burst ratio was varied by changing the number of sine waves operating in each burst cycle. The experiment was carried out by adjusting the 13 burst ratios from 0.01 (operation ratio of 1%) to 1 (operation ratio of 100%, continuous operation).

### 2.4.3. Burst Frequency

Table 3 lists the burst frequencies during the experiment. The input voltage, base frequency, and burst ratio were fixed at  $12 \text{ kV}_{\text{p-p}}$ ,  $f_{\text{base}} = 10,000 \text{ Hz}$ , and 0.5 (50% operation). The number of operating sine waves (the number of non-operating sine waves was also the same) of one burst cycle was changed to eight types between 1 and 5000 pulses. Consequently, the burst frequency varied over a wide range of  $f_{\text{burst}} = 1\text{--}5000 \text{ Hz}$ . Here, the non-dimensionalized burst frequency  $F^+$  was used.  $F^+$  was non-dimensionalized using the freestream velocity at the blade outlet,  $U_{\text{FS,out}}$ , and the blade chord length,  $C$ .

**Table 3.** Burst mode operation at various burst frequencies at fixed  $V_{\text{p-p}} = 12 \text{ kV}$ ,  $f_{\text{base}} = 10,000 \text{ Hz}$ ,  $BR = 0.5$ .

Burst Ratio, $BR$	Operation Number of Sine Waves in One Burst Cycle	Non-Operation Number of Sine Waves in One Burst Cycle	Operation Time at One Burst Cycle, $T_{\text{on}}$ (ms)	Non-Operation Time at One Burst Cycle, $T_{\text{off}}$ (ms)	Burst Frequency, $F_{\text{burst}}$ [Hz]	Non-Dimensionalized Burst Frequency, $F^+$
0.5	5000	5000	500	500	1	0.013
	1000	1000	100	100	5	0.063
	500	500	50	50	10	0.126
	100	100	10	10	50	0.629
	50	50	5	5	100	1.26
	10	10	1	1	500	6.29
	5	5	0.5	0.5	1000	12.6
	1	1	0.1	0.1	5000	62.9

The non-dimensionalized burst frequency  $F^+$  is defined as follows:

$$F^+ = f_{\text{burst}} \times \frac{C}{U_{\text{FS,out}}} \quad (6)$$

The non-dimensionalized burst frequency roughly shows the number of burst waveforms that occur when the freestream flows within a blade passage. For example, a burst frequency of  $F^+ = 1$  indicates that a burst wave occurs approximately once when the freestream flows within one blade passage. The experiment was carried out by adjusting the eight non-dimensionalized burst frequencies of  $F^+ = 0.013\text{--}62.9$ .

Figure 6 shows examples of the burst waveforms. Figure 6a–d show the continuous drive wave ( $BR = 1$ ) and the waveforms of  $F^+ = 6.29$ , 12.6, and 62.9 ( $BR = 0.5$ ). The red waveform in the figure shows the burst waveform for one burst time.

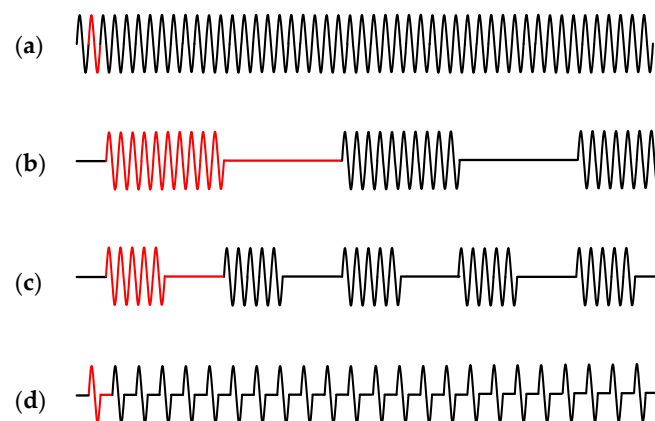


**Figure 6.** Examples of burst waves at non-dimensional burst frequencies of  $F^+ = 6.29$ , 12.6, 62.9 ( $BR = 0.5$ ): (a) continuous ( $BR = 1$ ); (b)  $F^+ = 6.29$  ( $BR = 0.5$ ); (c)  $F^+ = 12.6$  ( $BR = 0.5$ ); (d)  $F^+ = 62.9$  ( $BR = 0.5$ ).

### 3. Experimental Results and Discussion

Figure 7 shows an enlargement of the PIV measurement cross-section position shown in Figure 3a. The passages between the three blades of the turbine cascade were measured. Passages 1, 2, and 3 were located inside the blade, at the blade exit, and downstream of the blade, respectively. A plasma actuator was installed on the endwall upstream of the leading edge of the blade. The direction of flow induced by the plasma actuator is also shown in the figure.

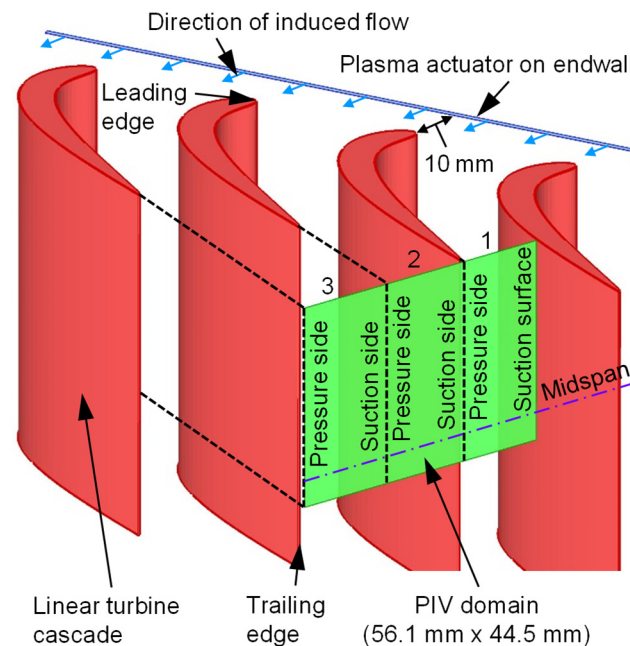


**Figure 7.** PIV measurement position.

#### 3.1. Effects of Burst Ratio

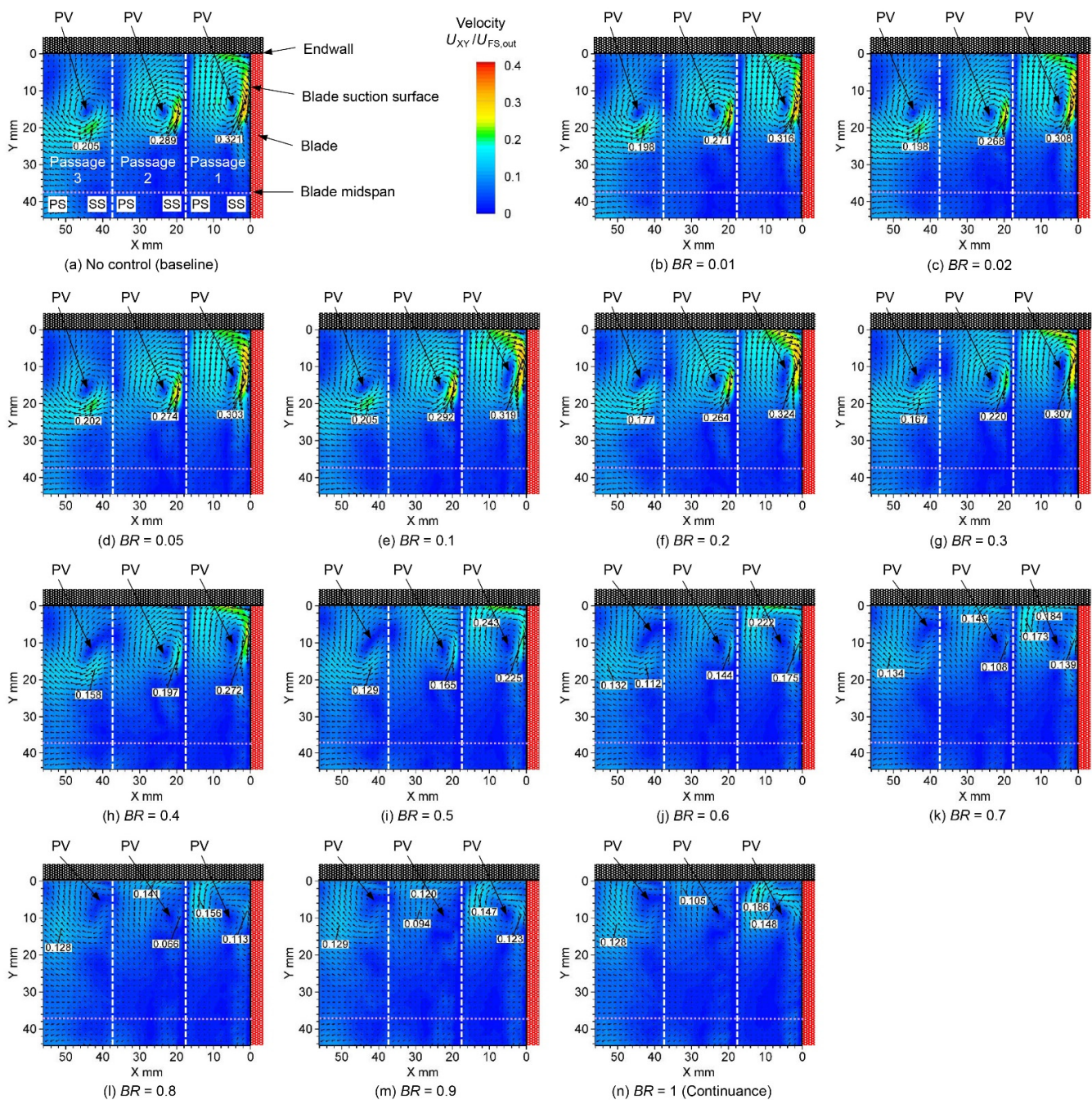
Figure 8 shows the velocity distribution, including the velocity peak values, at the linear turbine cascade outlet when the burst ratio of the plasma actuator was changed.

Figure 8a shows the velocity distribution at the no-control condition as a baseline. A large clockwise passage vortex (PV in the figure) was observed at each passage, and the secondary flow was strengthened when the passage vortex collided with the blade suction surface side. The peak velocities of passages 1, 2, and 3 at the inside of the blade, the blade exit, and downstream were 0.321, 0.289, and 0.205, respectively. The peak velocity of the passage vortex decreased as the vortex moved downstream.

Figure 8b–n show the velocity distributions when the burst ratio was changed as the plasma actuator was operated. As shown in Figure 8b–d, the peak velocity due to passage vortices in each blade decreased at very small drive conditions of 0.01–0.05 (operation of 1–5%). As seen in Figure 8e, with a burst ratio of 0.1 (10%), in passage 1 inside the blade, the high-velocity region moved to the top endwall side, and the location of the peak velocity moved to the endwall side. The peak velocity increased consecutively. This is because the interference between the vortex and the wall surface was strengthened by moving the position of the passage vortex to the endwall side. As seen in Figure 8f–j, with a burst ratio of 0.2–0.6 (20–60%), the high-velocity region of passage 1 gradually moved to the endwall. As seen in Figure 8k–n, with a burst ratio of 0.7–1 (70–100%), the high-velocity region of passage 1 moved from the endwall to the blade pressure side, and the peak location of the velocity also moved to the blade pressure side.

Figure 9 shows the peak velocity (local maximum velocity) of the passage vortex at various burst ratios shown in Figure 8. In passage 1 at the blade interior, shown in Figure 9a, a peak velocity decrease of 6% was observed at a very low BR of 0.05 (5% operation). Although the peak velocity increased temporarily at  $BR = 0.2$ , it decreased

gradually after  $BR = 0.2$ . The decrease in the peak velocity was up to 54% at  $BR = 0.9$ . At  $BR = 1$ , as shown in Figure 8n, the velocity reduction effect was slightly weaker than that at  $BR = 0.9$  because the velocity peak increased at the blade pressure side of the endwall. In passage 2 at the blade outlet, shown in Figure 9b, a peak velocity decrease of 7% was observed at a very low  $BR$  of 0.02 (2% operation). After increasing once at  $BR = 0.1$ , the peak velocity gradually decreased, and the peak velocity at  $BR = 1$  decreased by 64%. In passage 3 at the blade downstream, as shown in Figure 9c, the peak velocity decreased by 3% at  $BR = 0.02$ , and then, at  $BR = 0.1$ , it became virtually the same value as in the no-control case. Thereafter, the peak velocity gradually decreased until  $BR = 0.5$ , and it became approximately flat above  $BR = 0.5$ . A peak velocity decrease of 38% was maintained thereafter.



**Figure 8.** Velocity distributions of secondary flow at the outlet of the linear turbine cascade at various burst ratios.

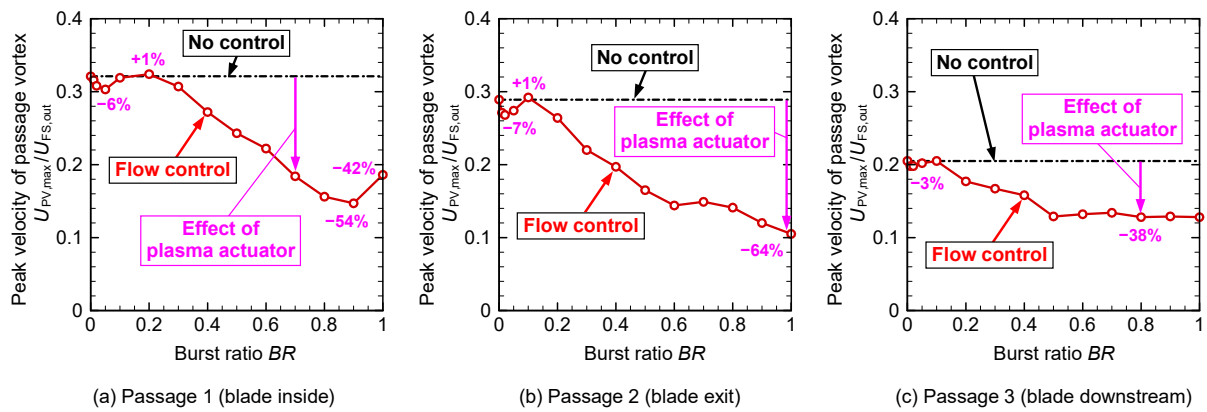


Figure 9. Peak velocity of passage vortex at various burst ratios.

Figure 10 shows the streamlines of the secondary flow at each burst ratio, which shows the center position of the passage vortex. The locations of the passage vortices are shown in each figure. Figure 10a shows the case with no flow control as a baseline. There were clockwise passage vortices in each passage, and their center positions were  $Y = 13$  mm,  $Y = 16$  mm, and  $Y = 15$  mm in passages 1, 2, and 3, respectively. As seen in Figure 10b–d, there was little change in the vortex center position at  $BR = 0.01$ – $0.05$ . In contrast, as shown in Figure 10e, at  $BR = 0.1$ , the center position of the passage vortex rose on the endwall side as  $BR$  increased. As seen in Figure 10j, a small counterclockwise vortex was generated on the blade suction side on the lower side of the passage vortex for  $BR = 0.6$ . An increase in the burst ratio resulted in a larger counterclockwise vortex.

Figure 11 shows plots of the center position of the passage vortex, as shown in Figure 10. The center positions at no control and continuous flow control ( $BR = 1$ ) are shown as black circles and white circles, respectively. Through continuous flow control, the center position of the passage vortex moved to the uppermost endwall side. In the burst operation cases, as the burst ratio increased, it gradually moved from the position of no control to the position of continuous flow control. The moving volume of the center position of the passage vortex by the flow control of the plasma actuator increased as the position moved downstream from passages 1, 2, and 3 at the blade inside, blade exit, and blade downstream, respectively.

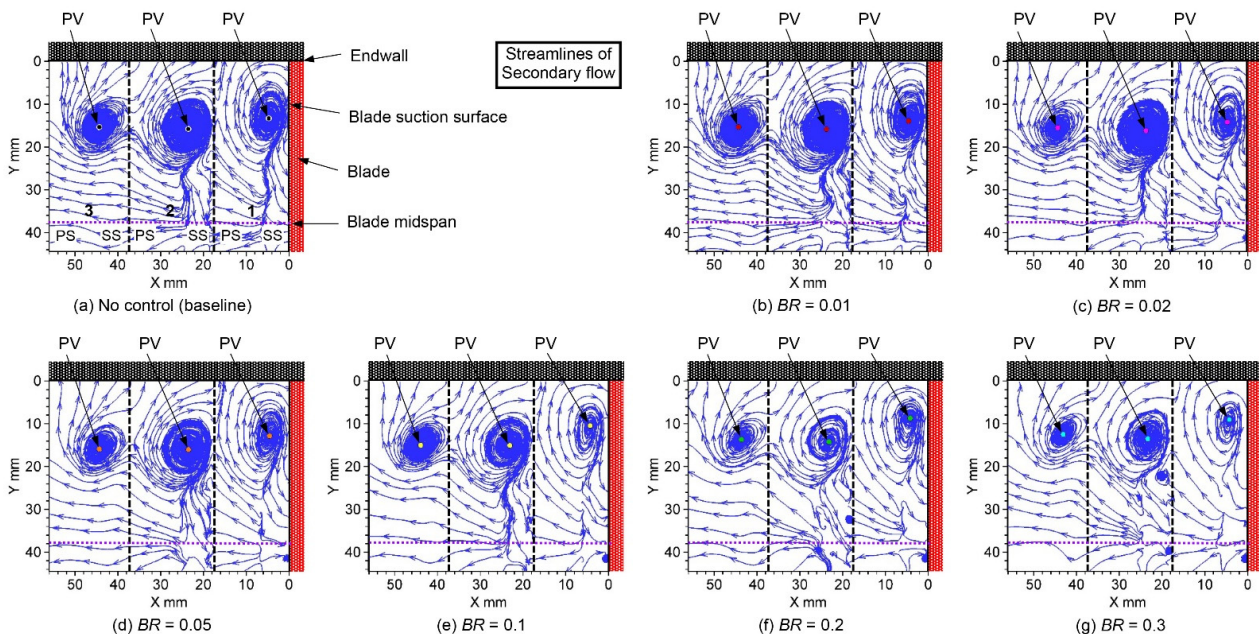


Figure 10. Cont.

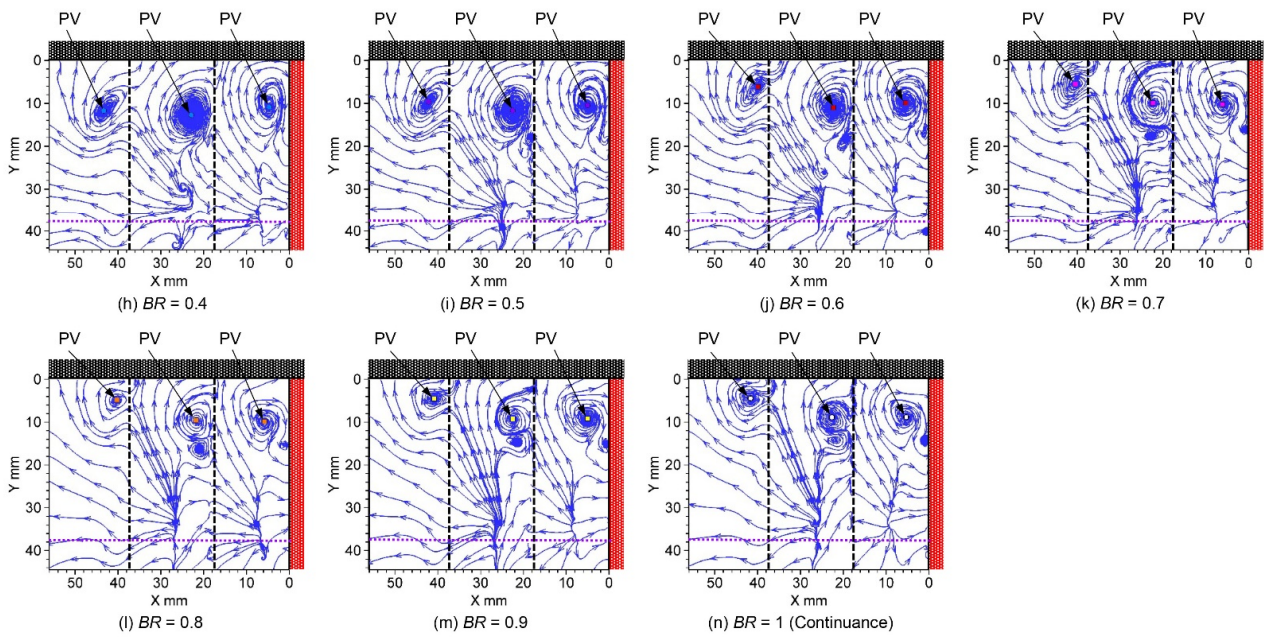


Figure 10. Streamlines of secondary flow at the outlet of the linear turbine cascade at various burst ratios.

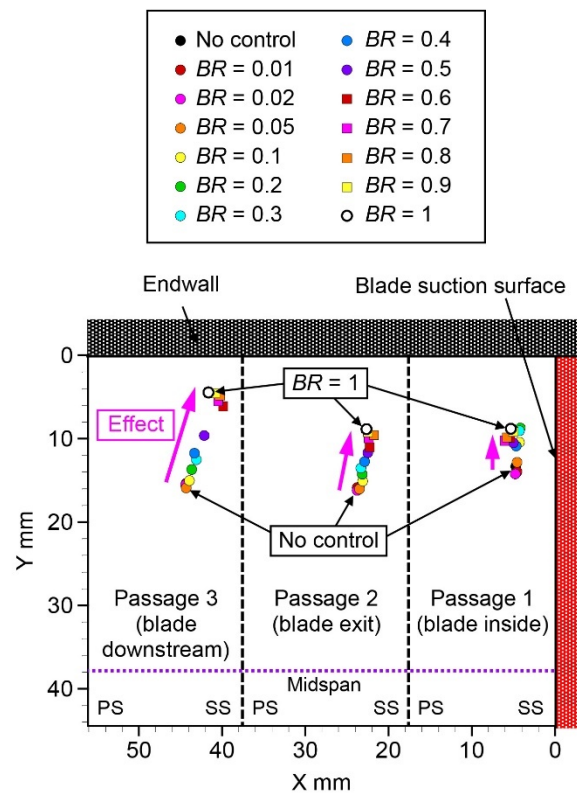


Figure 11. Plots of center positions of passage vortex at various burst ratios.

Figure 12 shows changes in the vertical direction (Y-direction) position of the vortex center shown in Figure 11. At passage 1 at the blade interior, shown in Figure 12a, the distance with the upper endwall surface at  $BR = 0.2$  decreased by 35% compared with the baseline. This value is approximately the same as the decrease at the continuous operation of  $BR = 1$ . In passage 2 at the blade exit, as shown in Figure 12b, the larger the burst ratio, the more closely the vortex center approached the upper endwall surface. In continuous operation ( $BR = 1$ ), the distance between the wall surface and the vortex center decreased

by 43%. This tendency was more pronounced in passage 3 at the blade downstream, as shown in Figure 12c. The vortex center location at passage 3 varied steeply at a burst ratio between 0.4 and 0.6. This tendency is also clearly confirmed in Figure 11. The distance between the endwall and the vortex center decreased by as much as 71% at  $BR = 0.9$ .

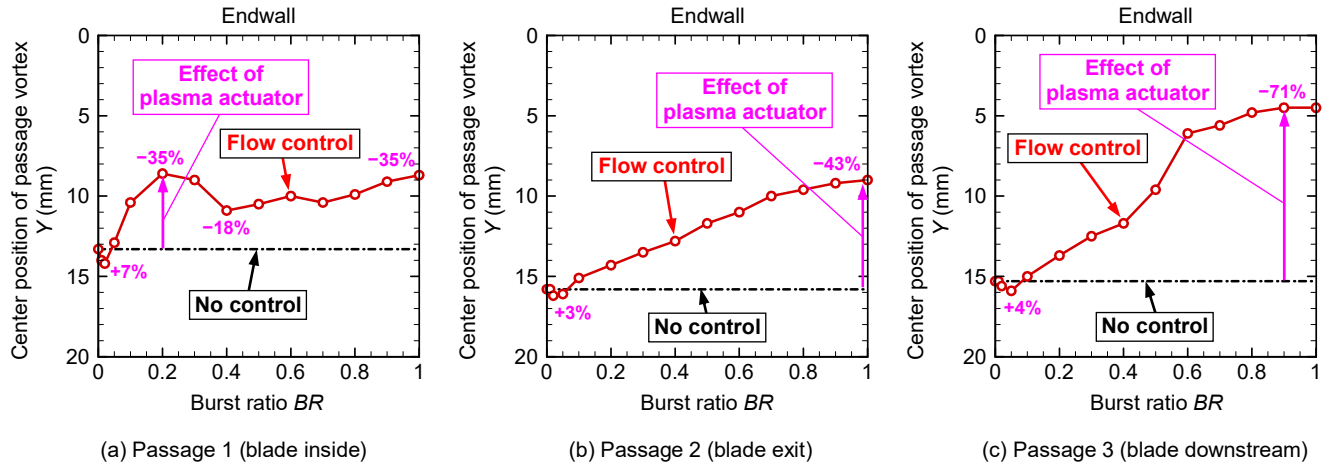
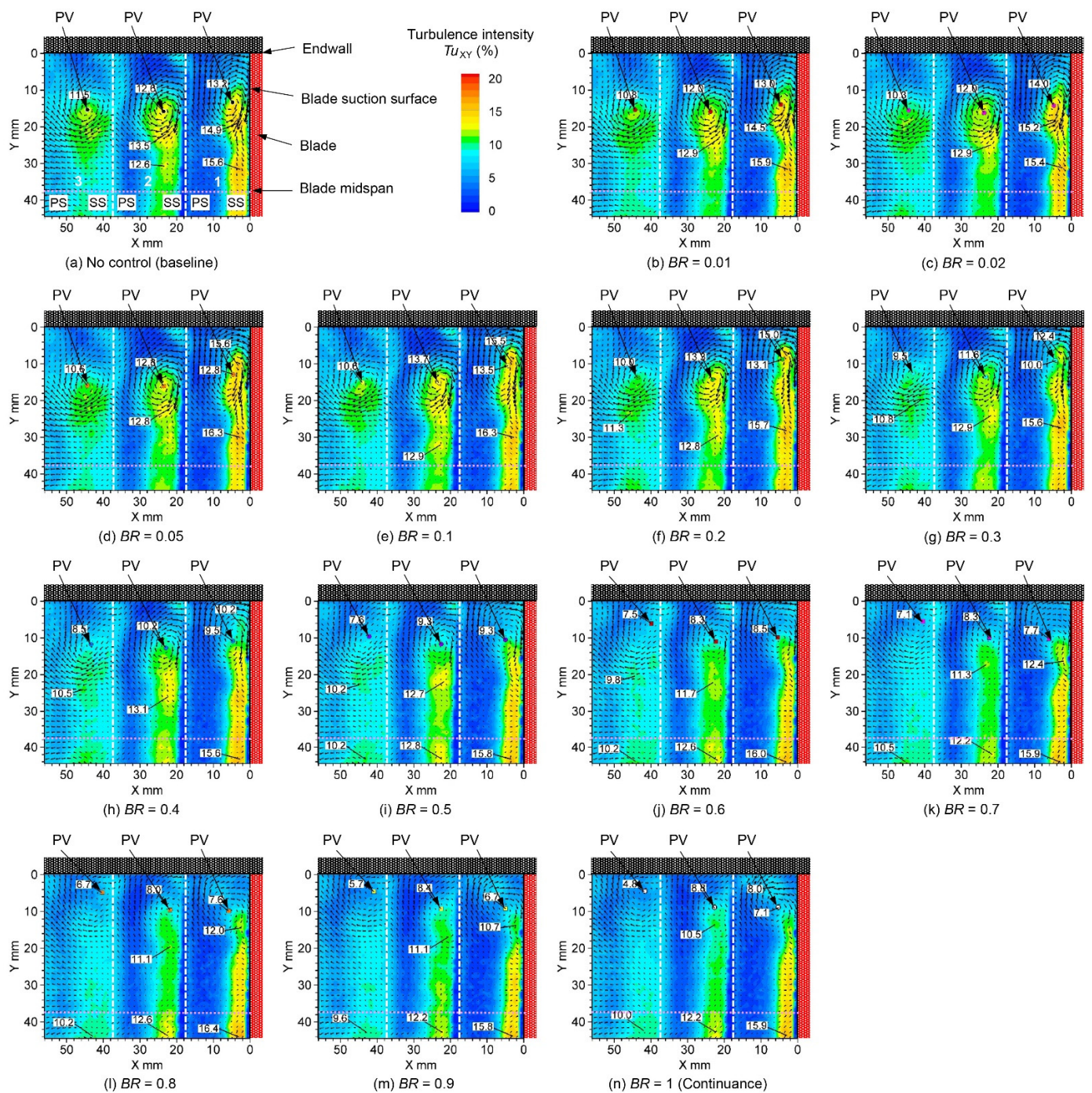


Figure 12. Center position of passage vortex at various burst ratios.

Figure 13 shows the distribution of the turbulence intensity at each burst ratio. Figure 13a shows the results without flow control. In each passage, the turbulence intensity was high at the center of the passage vortex. In passage 1 inside the blade, the turbulence intensity was 14.9% around  $Y = 20$  mm, where the passage vortex hit the blade suction side and rolled up, and the turbulence intensity was higher than that of the vortex center. On the lower side, at  $Y = 25$  mm, a region with high turbulence intensity was generated along the spanwise direction of the blade suction surface side, and the maximum turbulence intensity was 15.6%. The high turbulence intensity region along the blade suction surface side was caused by the separation of the boundary layer on the blade suction surface. Owing to the low Reynolds number condition, the horizontal width of the region of the high turbulence intensity caused by the flow separation was approximately one third of the blade pitch. At passage 2, the turbulence intensity at which the passage vortex rolled up from the blade suction surface was 13.5%, which was slightly weaker than that at passage 1. Similarly, the maximum turbulence intensity weakened to 12.6% in the region with high turbulence intensity, owing to the boundary layer separation.

Figure 13b shows the result of the plasma actuator being controlled by a burst ratio of 1% ( $BR = 0.01$ ). Compared to Figure 13a, each peak value of the turbulence intensity decreased, and it could be confirmed that it was effective even with only 1% operation of the plasma actuator. Up to a burst ratio of 0.2, as shown in Figure 13c–f, there was no significant change in the value of the maximum turbulence intensity, but the location of the maximum turbulence intensity moved to the upper endwall side. This appeared to be accompanied by the movement of the center position of the passage vortex to the upper endwall surface, as shown in Figure 11. As shown in Figure 13g, in passage 1 inside the blade, the position of the maximum turbulence intensity due to the passage vortex hardly changed, but the strength of the maximum turbulence intensity gradually decreased. In passage 2 at the blade exit and passage 3 at the blade downstream, the position of the maximum turbulence intensity of the passage vortex moved to the upper endwall side, and the strength of the turbulence intensity gradually weakened. In contrast, the separation region on the blade suction surface observed in passage 1 had a nearly constant strength of maximum turbulence intensity and maintained a value of approximately 16%. This separation region existed up to approximately  $Y = 30$  mm at no control; however, when the burst ratio was increased at flow control, it extended upward to approximately  $Y = 20$  mm. This is because the flow separation region expanded by weakening the passage vortex.



**Figure 13.** Turbulence intensity distributions of secondary flow at the outlet of the linear turbine cascade at various burst ratios.

Figure 14 shows how the turbulence intensity at the center position of the passage vortex of Figure 13 changes with the burst ratio. According to Figure 14a, at the blade interior, there was no change from no control ( $BR = 0$ ) to  $BR = 0.2$ , and it was virtually constant around 13%. At  $BR = 0.3$  or higher, the turbulence intensity of the vortex center gradually decreased as the burst ratio increased. At  $BR = 0.9$ , a decrease of up to 49% was observed. According to Figure 14b, at the blade exit, no effect was observed until  $BR = 0.2$ ; however, at  $BR = 0.3$  to  $0.6$ , the larger burst ratio resulted in smaller turbulence intensity. At  $BR = 0.6$  or higher, the turbulence intensity was maintained approximately constant, and a decrease of up to 37% was observed at  $BR = 0.8$ . In passage 3 at the blade downstream, as shown in Figure 14c, a decrease in the turbulence intensity of 10% was observed at

$BR = 0.02$ . The turbulence intensity was gradually decreased between  $BR = 0.1$  and 1, and the turbulence intensity decreased by up to 58% at  $BR = 1$ .

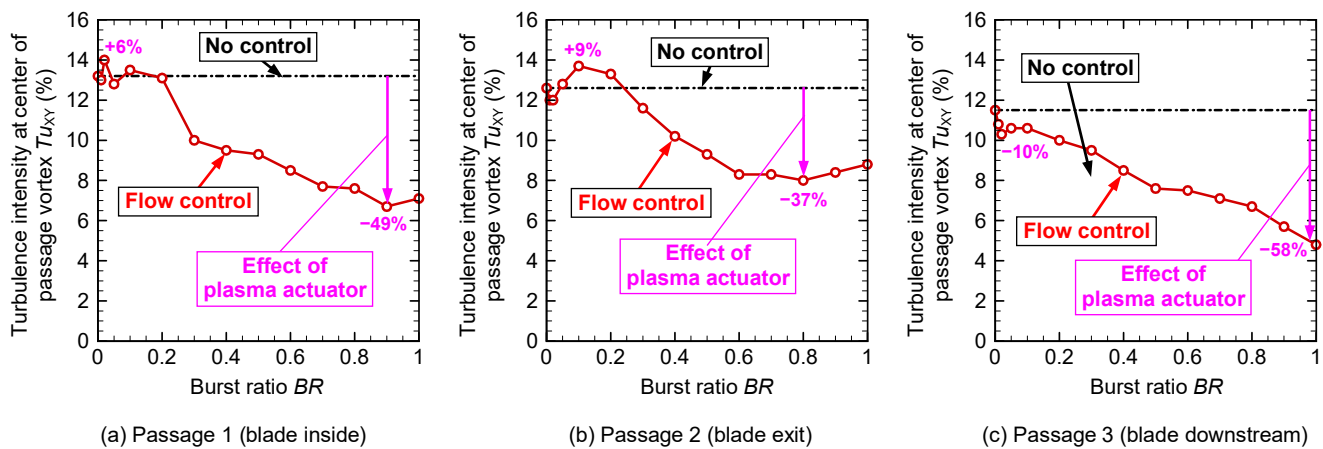


**Figure 14.** Turbulence intensity at the center of passage vortex at various burst ratios.

Figure 15 shows how the vorticity distribution changes with the burst ratio. At no control, as shown in Figure 15a, the area of the passage vortex had negative vorticity. The vorticity at the center of the passage vortex in passages 1, 2, and 3 was  $-720$ ,  $-630$ , and  $-500$   $s^{-1}$ , respectively. The strength of the negative vorticity decreased as the passage vortex moved downstream. The negative peak vorticity at passages 1, 2, and 3 was  $-830$ ,  $-690$ , and  $-540$   $s^{-1}$ , respectively, and their position and peak value were close to those at the center of the passage vortex. In passage 1, a strong counterclockwise vortex with positive vorticity occurred when the passage vortex hit the blade suction surface and rolled up. The maximum positive vorticity at passages 1, 2, and 3 was  $1160$ ,  $840$ , and  $250$   $s^{-1}$ , respectively, and it weakened rapidly as the counterclockwise vortex moved downstream.

Figure 15b shows the vorticity distribution at flow control of  $BR = 0.01$ . Both the vorticity at the center of the passage vortex and the negative peak vorticity were weaker than those at the no-control condition. Even plasma actuator operation at a slight burst ratio suppresses the passage vortex. As shown in Figure 15c, as the burst ratio decreased, the negative vorticity region decreased and moved to the upper endwall surface side.

In Figure 15, the value of the vorticity at the center of the passage vortex and the value of the negative peak vorticity are indicated. In the case of no control, as in Figure 15a, the position where the absolute value of the negative vorticity is the maximum is in close agreement with the center position of the passage vortex. In contrast, in the case of the control after Figure 15b, the position where the strength of the negative vorticity is the maximum peak is separated from the center of the passage vortex. It exists between the center position of the passage vortex and the upper endwall surface or blade suction surface. The reason for this is that the passage vortex weakens as the burst ratio increases, owing to the operation of the plasma actuator, and it approaches the upper endwall side and the blade suction surface side. Therefore, the interaction between the passage vortex and the upper endwall surface or the blade suction surface becomes stronger.

Figure 16 shows a negative vorticity at the center position of the passage vortex, as shown in Figure 15.

As shown in Figure 16a, the magnitude of the vorticity suddenly weakened at a burst ratio as low as  $BR = 0.1$ . The magnitude of vorticity was reduced by as much as 27% at  $BR = 0.1$  (10% operation). Although the absolute value of the vorticity increased temporarily at  $BR = 0.2$ , this seemed to be because the center of the passage vortex moved to the upper endwall side, and the interference between the vortex and the endwall surface intensified, as shown in Figure 12a. From  $BR = 0.2$  to 0.5, the strength of the vorticity rapidly weakened, and it decreased by as much as 67% at  $BR = 0.6$ . After  $BR = 0.6$ , the vorticity remained practically constant until  $BR = 0.8$ . After  $BR = 0.8$ , the strength of the

vorticity tended to increase gradually, and the decrease became 54% at  $BR = 1$ . This seemed to be due to the fact that the vortex center moved further to the upper endwall side, as observed in Figure 12a, and the interaction between the passage vortex and the endwall surface intensified.

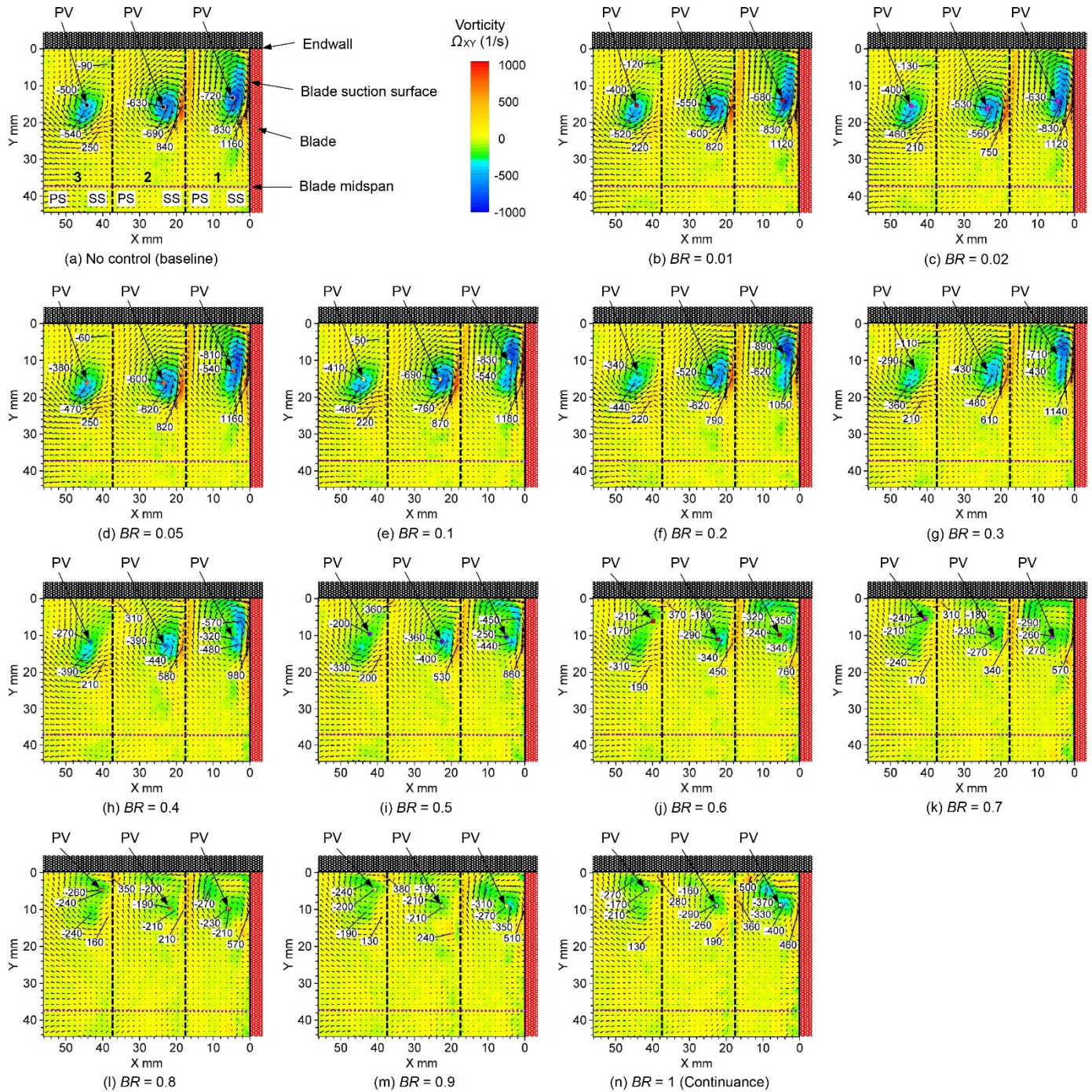


**Figure 15.** Vorticity distributions of secondary flow at the outlet of the linear turbine cascade at various burst ratios.

As seen in Figure 16b, the vorticity at flow control of  $BR = 0.02$  (2% operation) was reduced by 16% from that at no control. Subsequently, the vorticity at  $BR = 0.1$  was increased by 10%. This is because the vortex center at  $BR = 0.1$  moved to the upper endwall side, as observed in Figure 11b. Simultaneously, as observed in Figure 12b, the turbulence intensity at  $BR = 0.1$  was also 9% higher than that at no control. After  $BR = 0.2$ , the vorticity gradually

weakened, and the vorticity at  $BR = 0.8$  was decreased by 70%. At  $BR = 0.9$  and  $BR = 1$ , the vorticity increased slightly, because the center position of the vortex moved further to the upper endwall side, as shown in Figure 12b, and the interference between the passage vortex and the endwall surface intensified. This can also be observed from the increase in the turbulence intensity, as shown in Figure 14b.

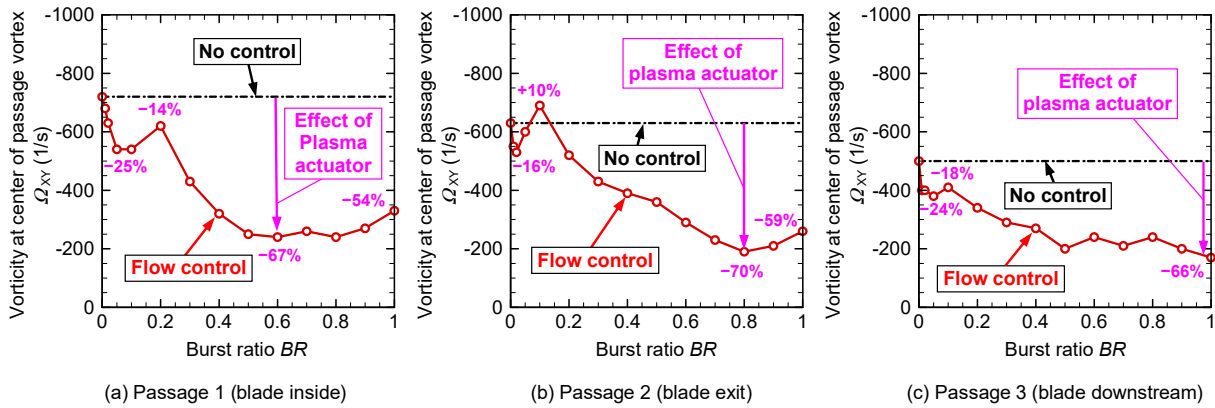


Figure 16. Vorticity at the center of passage vortex at various burst ratios.

As seen in Figure 16c, the vorticity decreased rapidly with very slight operation at  $BR = 0.01$ , and it was reduced by as much as 24% at  $BR = 0.05$ . Concurrently, the center position of the passage vortex shown in Figure 12c moved downward slightly, away from the upper endwall surface. The magnitude of the vorticity increased slightly at  $BR = 0.1$ . The vortex center position shown in Figure 12c at  $BR = 0.1$  moved to the upper endwall side, and the interaction between the endwall surface and the vortex was temporarily intensified. From  $BR = 0.2$  to  $0.5$ , the vorticity gradually decreased. From  $BR = 0.5$  to  $0.8$ , the vorticity was nearly flat, and at  $BR = 0.9$  or higher, the magnitude of the vorticity decreased again. The magnitude of the vorticity at  $BR = 1$  was reduced by 66%.

Figure 17 shows the negative peak vorticity shown in Figure 15. The overall trend is similar to that shown in Figure 16. In Figure 17a, the vorticity from  $BR = 0$  to  $BR = 0.2$  is virtually constant; however, it decreases sharply after  $BR = 0.2$ . The magnitude of the negative peak vorticity decreases by 67% at  $BR = 0.8$ . In Figure 17b, the vorticity falls sharply at  $BR = 0.02$  (19% reduction), and then increases once at  $BR = 0.1$ . The vorticity gradually decreased after  $BR = 0.2$  and showed a decrease of up to 70% at  $BR = 0.8$ . In Figure 17c, the vorticity drops sharply at  $BR = 0.02$  (15% reduction), then slightly increases at  $BR = 0.1$ , gradually decreases after  $BR = 0.1$ , and decreases by 56% at  $BR = 0.7$ . After  $BR = 0.7$ , the vorticity remains practically constant. Finally, the magnitude of the vorticity at  $BR = 1$  is slightly increased, and the reduction in the vorticity is 50%.

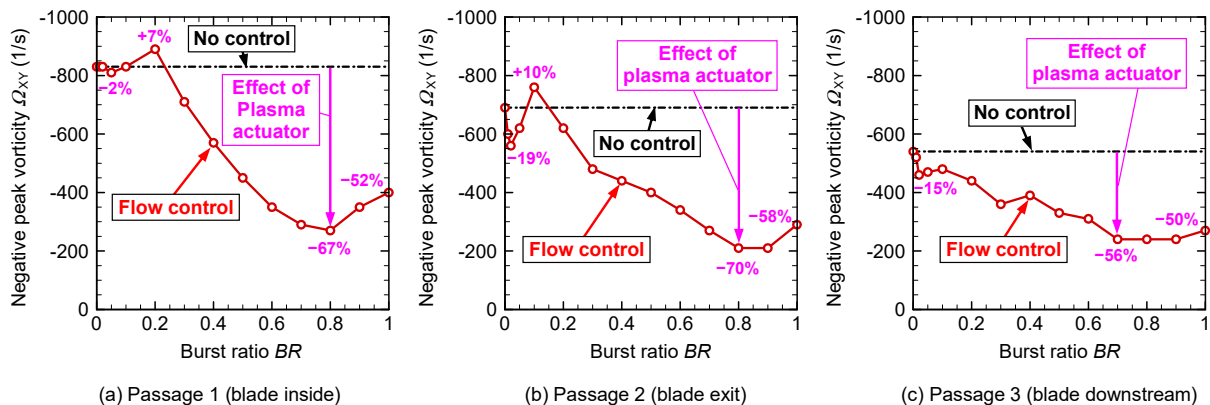
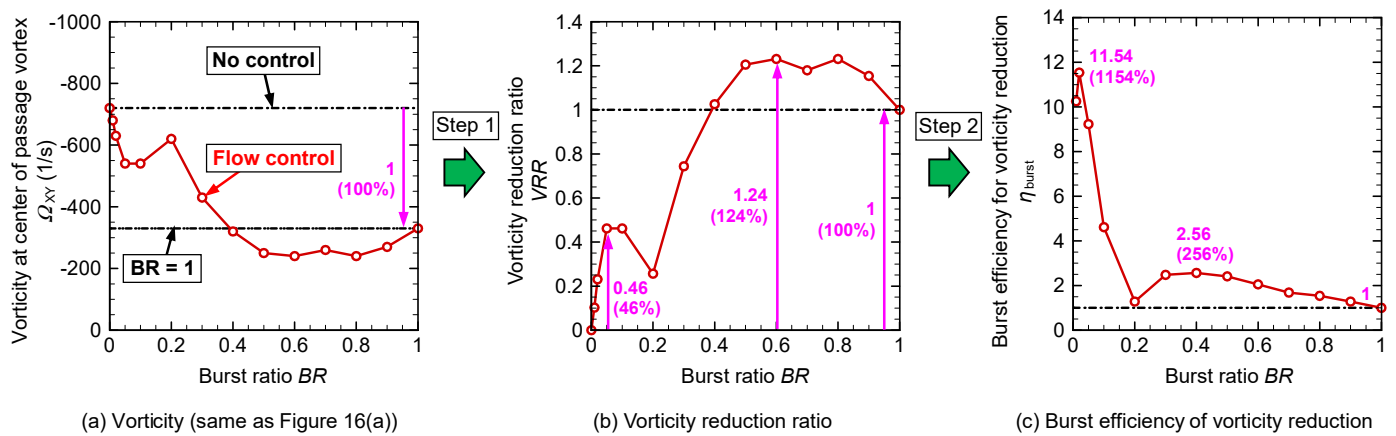


Figure 17. Negative peak vorticity at various burst ratios.

As shown in Figures 8–17, the effect of the burst ratio on the burst operation of the plasma actuator was examined. The higher the burst ratio, the weaker the passage vortex and the more the passage vortex moves to the upper endwall surface and blade suction surface side. However, it was clarified that the velocity distribution, streamlines of the secondary flow, turbulence intensity distribution, and vorticity distribution did not necessarily change proportionally with the change in the burst ratio and that the turbulence intensity and vorticity decreased or increased temporarily with the movement of the passage vortex and the interaction between the passage vortex and the upper endwall surface.

To consider and discuss the energy consumption during burst mode operation, the vorticity reduction ratio (*VRR*) and burst efficiency ( $\eta_{burst}$ ) were analyzed. The analysis process is illustrated in Figure 18. Figure 18a shows a representation of the vorticity at the center of the passage vortex in passage 1 at the blade interior at various burst ratios, as shown in Figure 16a.



**Figure 18.** Burst efficiency analyzed by the vorticity at the center of passage vortex in passage 1 at various burst ratios.

As the first step, *VRR* was calculated as follows:

$$VRR = \frac{\Omega_{XY,NC} - \Omega_{XY}}{\Omega_{XY,NC} - \Omega_{XY,BR=1}} \tag{7}$$

where  $\Omega_{XY,NC}$  and  $\Omega_{XY,BR=1}$  are the vorticities at the center of the passage vortex at no control and in continuous operation mode ( $BR = 1$ ), respectively. The calculated results are shown in Figure 18b. In this figure, the vorticity reduction ratio in continuous mode operation,  $BR = 1$ , is set to 1 (100%) as a reference. There were two peaks of *VRR*. One was at  $BR = 0.05$  (5% operation), where the *VRR* becomes 0.46 (46%). The other was at  $BR = 0.6$  (60% operation), where the *VRR* becomes 1.24 (124%) reduction. These results indicate that burst mode operation by a few percent results in a larger vorticity reduction, and burst mode operation with a burst ratio from 50% to 90% results in a higher vorticity reduction compared with continuous mode operation.

In the second step, the efficiency of the burst mode for the vorticity at the center of the passage vortex,  $\eta_{burst}$ , was calculated as follows:

$$\eta_{burst} = \left( \frac{\Omega_{XY,NC} - \Omega_{XY}}{\Omega_{XY,NC} - \Omega_{XY,BR=1}} \right) / BR = \frac{VRR}{BR} \tag{8}$$

The calculated results are shown in Figure 18c. Because the electric energy consumption of the plasma actuator in burst mode operation is proportional to the burst ratio [22], the burst efficiency,  $\eta_{burst}$ , indicates the efficiency of the vorticity reduction effect considering the electric energy consumption of the plasma actuator. In Figure 18c, two high peaks

of burst efficiency are observed. One peak is located at a very low burst ratio of  $BR = 0.05$  (5% operation), where the burst efficiency is as much as 11.54 (1154%), compared with that in continuous mode operation. The other peak is located at  $BR = 0.4$  (40% operation), where the burst efficiency is 2.56 (256%). In this figure, the burst efficiency at any burst ratio is greater than 1 (100%). This result indicates that the burst mode operation of the plasma actuator is more effective than continuous mode operation in terms of electric energy consumption.

There is no other study concerning the burst mode operation of plasma actuators for the reduction of the passage vortex in the turbine blade. Therefore, the results in this study were compared with burst mode operation for the reduction of the flow separation on the suction surface of single airfoils. Corke and Post [4] reported that only  $BR = 0.1$  (10%) was sufficient for the separation control of an airfoil. Bernard et al. [5] also found that the lift force on an airfoil was enhanced at  $F^+ = 1.0$  and  $BR = 0.06$  (6%), while the electric power consumption was significantly reduced compared to steady actuation. They described that the momentum transfer at such low  $BR$  is presumably reduced compared to larger  $BR$  and continuous operation. The amount of momentum transfer to the boundary layer of the airfoil is not the primary parameter for effective control. It was suspected that the periodic perturbations imparted by the plasma discharge drove the performance of the control. With the passage vortex reduction control of turbine blades in this study, a similar tendency was observed. There were two peaks in the high burst efficiency of the vorticity reduction at a very low  $BR$  of 0.05 (5%) and at a relatively higher  $BR$  of 0.4 (40%). The first peak in high burst efficiency at low  $BR$  is considered to be generated by the perturbation of the inlet boundary layer of the turbine cascade. Hence, the second peak in high burst efficiency at high  $BR$  is due to the synergistic effect of both the perturbation and momentum transfer to the inlet boundary layer. These two points offer new perspectives on the active flow control of the passage vortex in turbomachinery.

### 3.2. Effects of Burst Frequency

Figure 19 shows the effect of the difference in burst frequency on the measured velocity distribution.

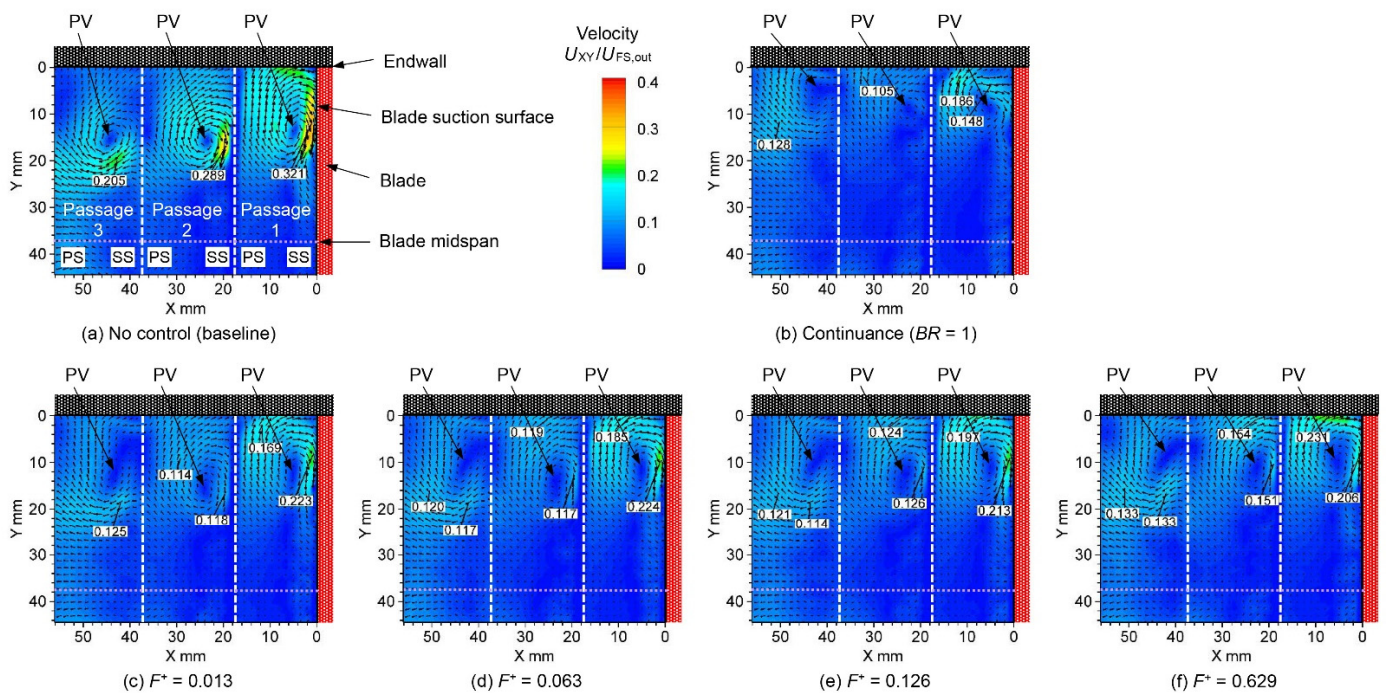
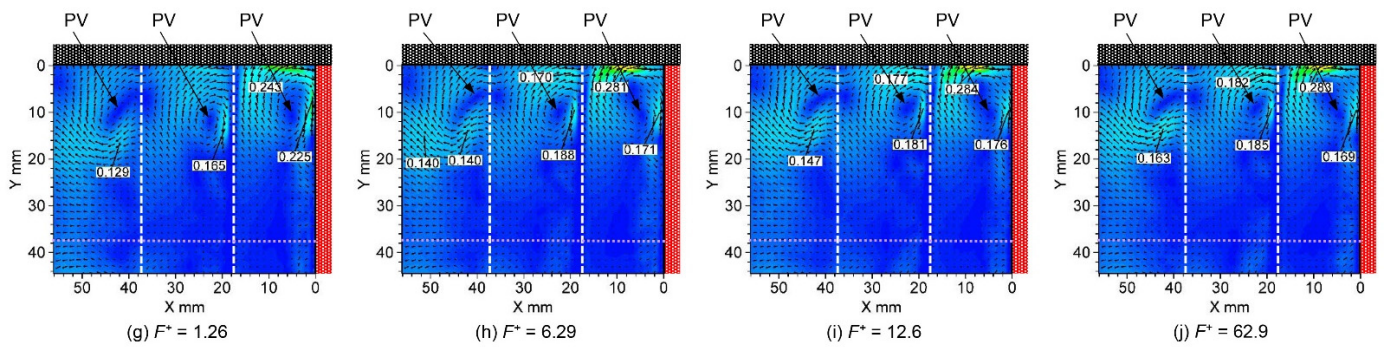


Figure 19. Cont.



**Figure 19.** Velocity distributions of secondary flow at the outlet of the linear turbine cascade at various burst frequencies ( $BR = 0.5$ ).

Figure 19a shows the velocity distribution with no control, and Figure 19b shows the velocity distribution with flow control during continuous operation ( $BR = 1$ ). Figure 19a,b are the same as Figure 8a,n, respectively.

Figure 19c–j show the velocity distributions when  $F^+$  is changed under a 0.5 fixed burst ratio. In Figure 19c, at the lowest burst ratio,  $F^+ = 0.013$ , the center position of the passage vortex is close to that in Figure 19a with no control. However, the peak value of the velocity of the secondary flow is close to that shown in Figure 19b for the continuous flow control of  $BR = 1$ . As shown in Figure 19d, the center position of the passage vortex moved to the upper endwall side as the burst frequency increased. Through this movement, the interaction between the passage vortex and the upper endwall becomes stronger, and the maximum peak velocity of the secondary flow is generated at the location where the passage vortex hits the upper endwall surface. In contrast, the interaction between the passage vortex and blade suction surface side becomes weaker, and the peak value of the velocity at the location where the passage vortex rolls from the blade suction surface side tends to be smaller.

Figure 20 shows how the peak value of the velocity generated by the passage vortex in Figure 19 changes with the burst frequency increase. In each figure, the value at no control in Figure 19a is shown by the black dash-dot-dash line, and the value at flow control by the continuous operation,  $BR = 1$ , in Figure 19b is shown by the black dash-dot-dot-dash line.

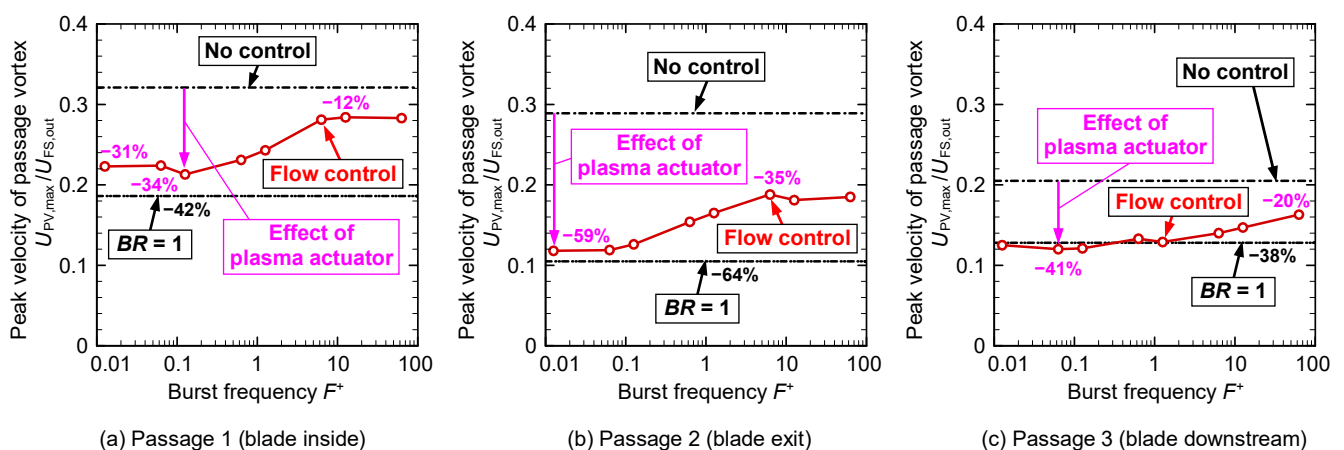


**Figure 20.** Peak velocity of passage vortex at various burst frequencies ( $BR = 0.5$ ).

In Figure 20a, at the lower burst frequency of  $F^+ = 0.013$ – $0.126$ , the peak velocity is reduced more than that at no control, and a reduction of 34% is observed at  $F^+ = 0.126$ , which is closest to the baseline (represented by the black dash-dot-dot-dash line) at the continuous operation of  $BR = 1$ . When the burst frequency was  $F^+ = 0.126$ – $6.29$ , the peak value of the velocity tended to increase with the burst frequency. This is because,

as observed in Figure 19, the center position of the passage vortex moved to the upper endwall side, and the interaction between the vortex and endwall surface became stronger. Hence, at  $F^+ = 6.29\text{--}62.9$ , the peak value of the velocity was nearly constant.

In Figure 20b, the same tendency as in passage 1 is observed. At  $F^+ = 0.013\text{--}0.063$ , the reduction in the peak value of the velocity was large, and a reduction of as much as 59% was observed, which is quite close to the value of continuous flow control ( $BR = 1$ ). At  $F^+ = 0.063\text{--}6.29$ , the peak velocity due to passage vortices gradually increased; then, at  $F^+ = 6.29\text{--}62.9$ , the peak velocity was nearly constant.

In Figure 20c, at the burst frequency  $F^+ = 0.063\text{--}1.26$ , the peak velocity is virtually constant, and the value is coincident with that during continuous operation ( $BR = 1$ ). The peak velocity was reduced by up to 41%. Above  $F^+ = 1.26$ , the peak velocity gradually increased. The peak velocity at  $F^+ = 62.9$  was nearly in the middle position between no control and continuous flow control.

In any passage, the peak velocity tended to increase as the burst frequency increased. This is because the passage vortex moved to the upper endwall side as the burst frequency increased, and the interaction between the passage vortex and endwall surface became stronger.

Figure 21 shows the streamlines of the secondary flow when the burst frequency changes. Figure 21a,b show the streamline distributions with no control and continuous flow control, respectively, and are the same as Figure 10a,n. Figure 21c,j show the results when the burst frequency was changed. As the burst frequency increased, the center position of the passage vortex moved to the upper endwall side.

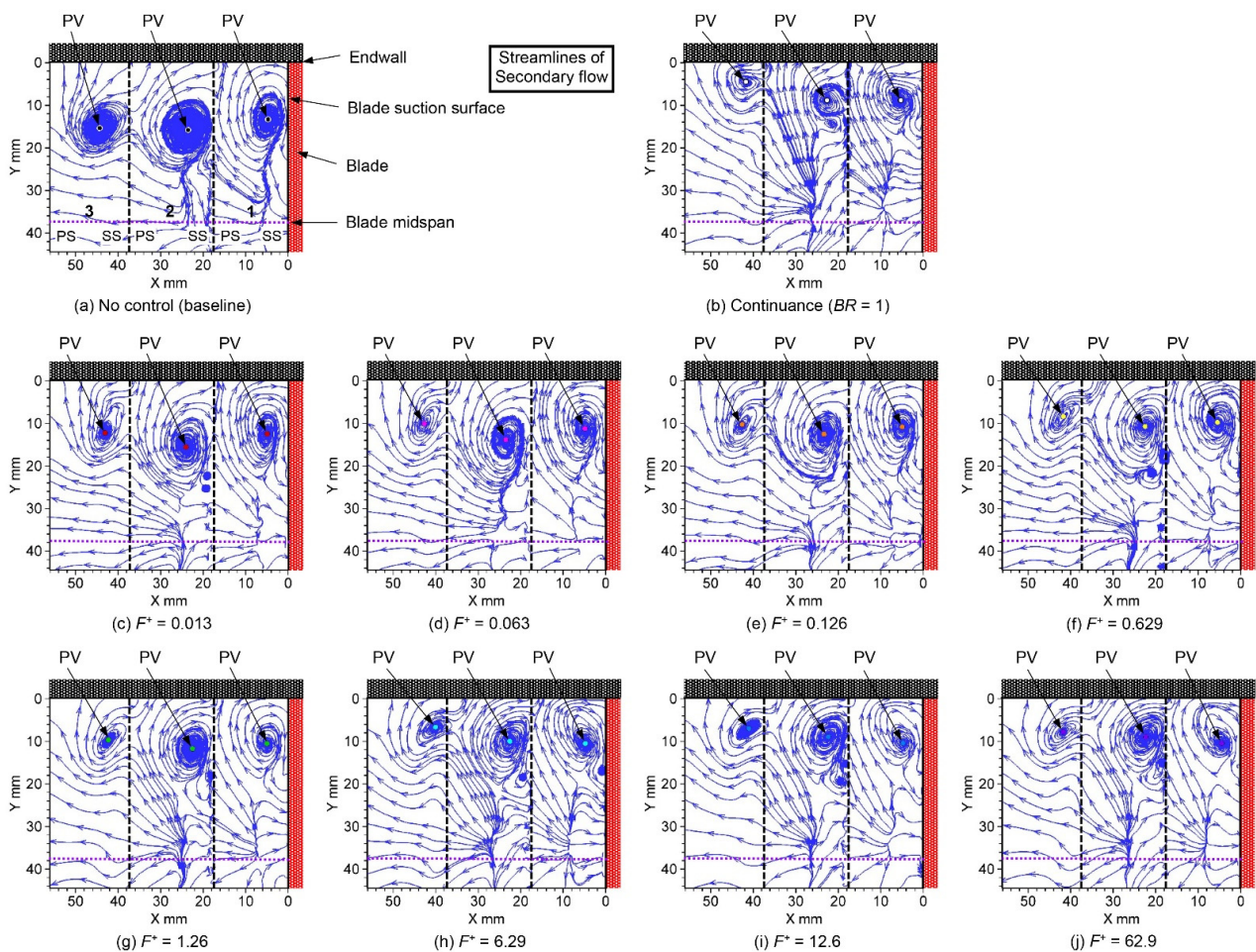


**Figure 21.** Streamlines of secondary flow at the outlet of the linear turbine cascade at various burst frequencies ( $BR = 0.5$ ).

Figure 22 shows a plot of the center position of the passage vortex shown in Figure 21. The black circle in the figure shows the vortex center with no control, and the white circle shows the vortex center during continuous operation ( $BR = 1$ ). The center position at the lowest burst frequency,  $F^+ = 0.063$  (red circle), is closest to that of the no-control case (black circle). As the burst frequency increased, the center position gradually approached that of the continuous operation flow control (white circle). When passages 1–3 are compared, the movement to the upper endwall side of the vortex center location increases as the vortex moves downstream at passage 1 inside the blade, passage 2 at the blade exit, and passage 3 at the blade downstream, which means that the flow control effect of the plasma actuator becomes higher downstream.

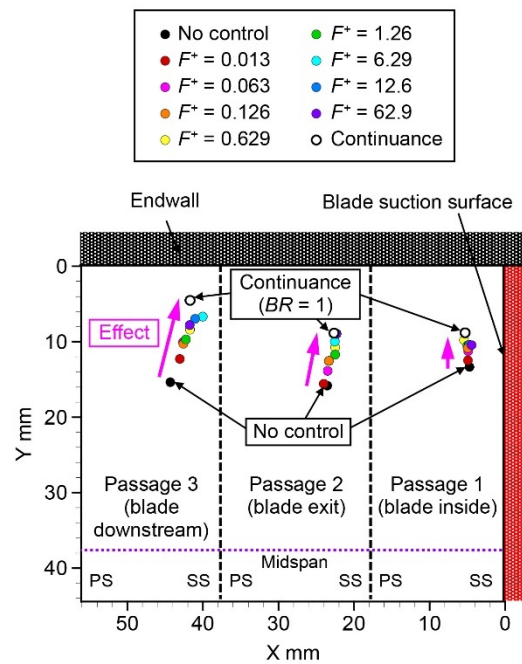


Figure 22. Plots of center positions of passage vortex at various burst frequencies ( $BR = 0.5$ ).

Figure 23 shows how the vertical distance ( $Y$ -coordinate) from the upper endwall surface at the center position of the passage vortex in Figure 22 changes with the burst frequency.

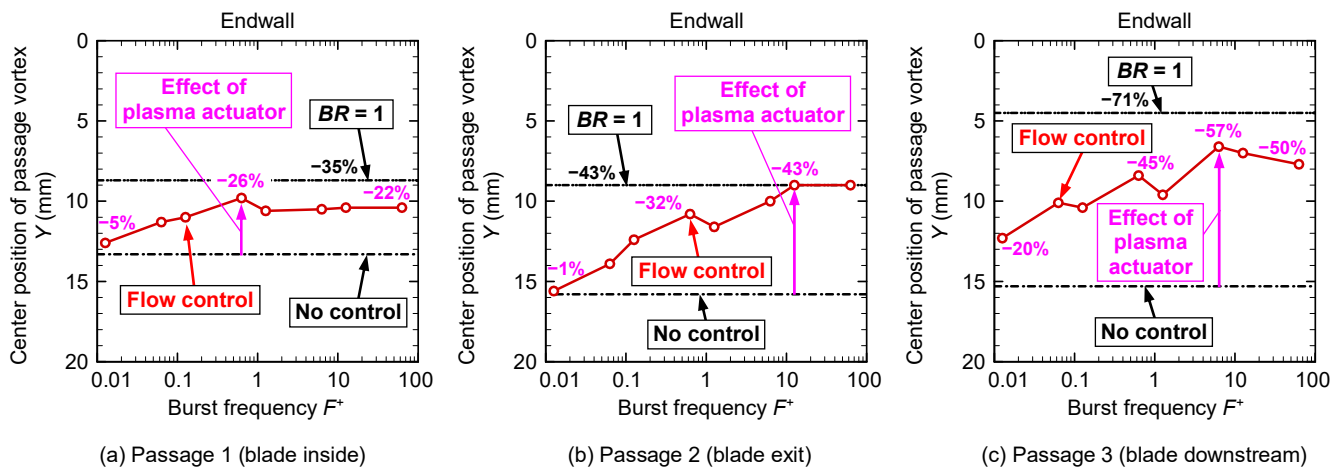


Figure 23. Center position of passage vortex at various burst frequencies ( $BR = 0.5$ ).

In Figure 23a, at the lowest burst frequency of  $F^+ = 0.013$ , the center position of the passage vortex is far from the upper endwall surface, and it is close to the center position with no control. At a burst frequency of  $F^+ = 0.013$ – $0.629$ , a higher burst frequency results

in a smaller distance between the vortex center position and the upper endwall surface. At  $F^+ = 0.629$ , the distance between the vortex center and the upper endwall surface was reduced by 26%, and it was close to the vortex center position in continuous flow control ( $BR = 1$ ). At a burst frequency of  $F^+ = 1.26$  or higher, the vortex center position remained virtually constant.

In Figure 23b, the vortex center position at  $F^+ = 0.013$  is practically the same as that at no control. As the burst frequency increased, the vortex center position gradually moved to the upper endwall side, and at  $F^+ = 12.6$ , the distance between the vortex center and the endwall decreased by 43% compared with that at no control, and it became the same as that at continuous flow control ( $BR = 1$ ). Subsequently, it maintained the same value at  $F^+ = 62.9$ .

Figure 23c shows that  $Y$  had the largest value at  $F^+ = 0.013$ . As the burst frequency increased, the vortex center position gradually moved to the upper endwall side. At  $F^+ = 6.29$ ,  $Y$  decreased by as much as 57% compared with  $Y$  at no control. After  $F^+ = 12.6$ ,  $Y$  tended to increase slightly.

Figure 24 shows how the turbulence intensity distribution changes with the change in burst frequency. Figure 24a,b are the same as Figure 13a,n at no control ( $BR = 0$ ) and continuous flow control ( $BR = 1$ ), respectively.

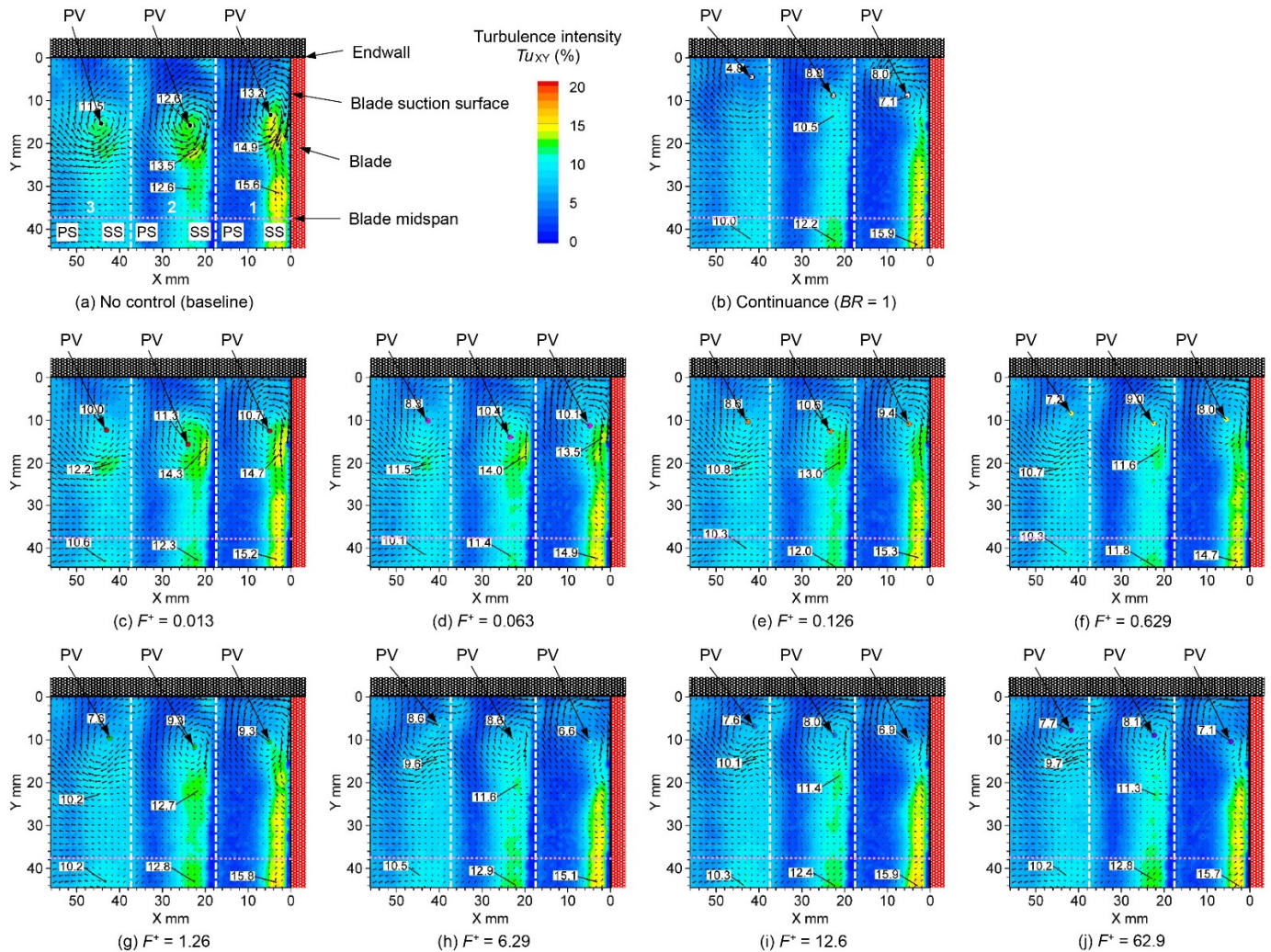


Figure 24. Turbulence intensity distributions of secondary flow at the outlet of the linear turbine cascade at various burst frequencies ( $BR = 0.5$ ).

Figure 24c–j show the distributions of the turbulence intensity when the burst frequency  $F^+$  is changed under conditions where the burst ratio is fixed at 0.5. When the smallest burst frequency of  $F^+ = 0.013$  is used, as shown in Figure 24c, the turbulence intensity distribution is closer to that with no control, shown in Figure 24a, than that with continuous flow control, as shown in Figure 24b. As shown in Figure 24d, as the burst frequency increases, the turbulence intensity distribution approaches that of the continuous flow control, shown in Figure 24b. At burst frequency  $F^+ = 6.29$ , as shown in Figure 24h, the turbulence intensity distribution is most similar to that of the continuous flow control, shown in Figure 24b.

Figure 25 shows how the turbulence intensity at the center position of the passage vortex of Figure 24 changes with the change in the burst frequency. The value at no control is shown by the black dash-dot-dash line, and the value at continuous flow control ( $BR = 1$ ) is shown by the black dash-dot-dot-dash line.

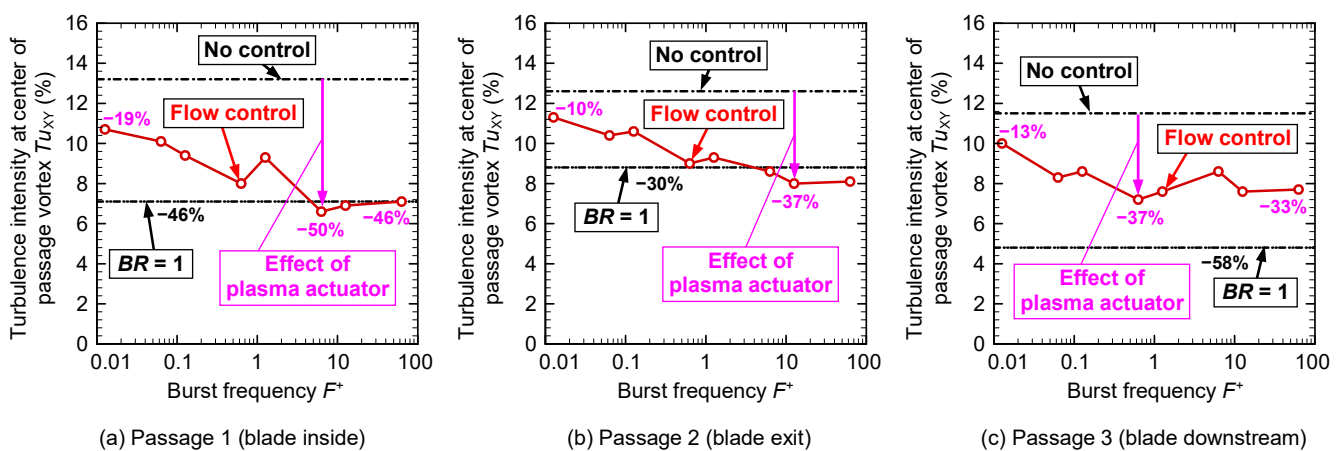


Figure 25. Turbulence intensity at the center of passage vortex at various burst frequencies ( $BR = 0.5$ ).

In Figure 25a, at a low burst frequency, the turbulence intensity is located in the middle, between the value at no control and the value at continuous flow control. The higher the burst frequency, the smaller the turbulence intensity, and, at  $F^+ = 6.29$ , there is a reduction of 50% compared with that at no control, which nearly agrees with the black dash-dot-dot-dash line of continuous flow control. Even if the burst frequency increased further, there was not much change.

Figure 25b shows a similar tendency. At a low burst frequency, the turbulence intensity at the center of the passage vortex was closer to that at no control; however, it gradually decreased as the burst frequency increased. At  $F^+ = 0.629$ , the turbulence intensity was in close agreement with the value for continuous flow control. The turbulence intensity at  $F^+ = 12.6$  was reduced by 37% compared with that at no control.

As shown in Figure 25c, the turbulence intensity at a low burst frequency was close to the value at no control, and it decreased gradually as the burst frequency increased. At  $F^+ = 0.629$ , a reduction in the turbulence intensity of 37% was observed compared with the no-control condition. However, unlike passages 1 and 2, even at high burst frequencies, the turbulence intensity remained higher than that under continuous flow control.

Figure 26 shows how the vorticity distribution of the secondary flow changes with the change in the burst frequency. In the figure, the vortex at the center position of the passage vortex and the positive and negative peak values of the vorticity are recorded. Figure 26a,b are the vorticity distributions at no control and continuous flow control ( $BR = 1$ ), respectively, and they are the same as Figure 15a,n.

Figure 26c shows the vorticity distribution at the lowest burst frequency of  $F^+ = 0.013$ , and the distribution is similar to that with no control, as shown in Figure 26a. However, the peak value of the vorticity is close to that of the continuous flow control ( $BR = 1$ ), as shown in Figure 26b. In passage 1, the vorticity reaches a negative peak value when the

passage vortex hits the blade suction surface side. In addition, there is a positive peak value of the vorticity in the vicinity of the blade suction surface. As shown in Figure 26d, the higher burst frequency results in the movement of the negative vorticity region to the upper endwall surface side because of the movement of the passage vortex to the upper endwall. In passage 1, after  $F^+ = 6.29$ , as shown in Figure 26h, a region in which the vorticity is strongly negative is formed near the upper endwall surface, because the passage vortex approaches the upper endwall surface.

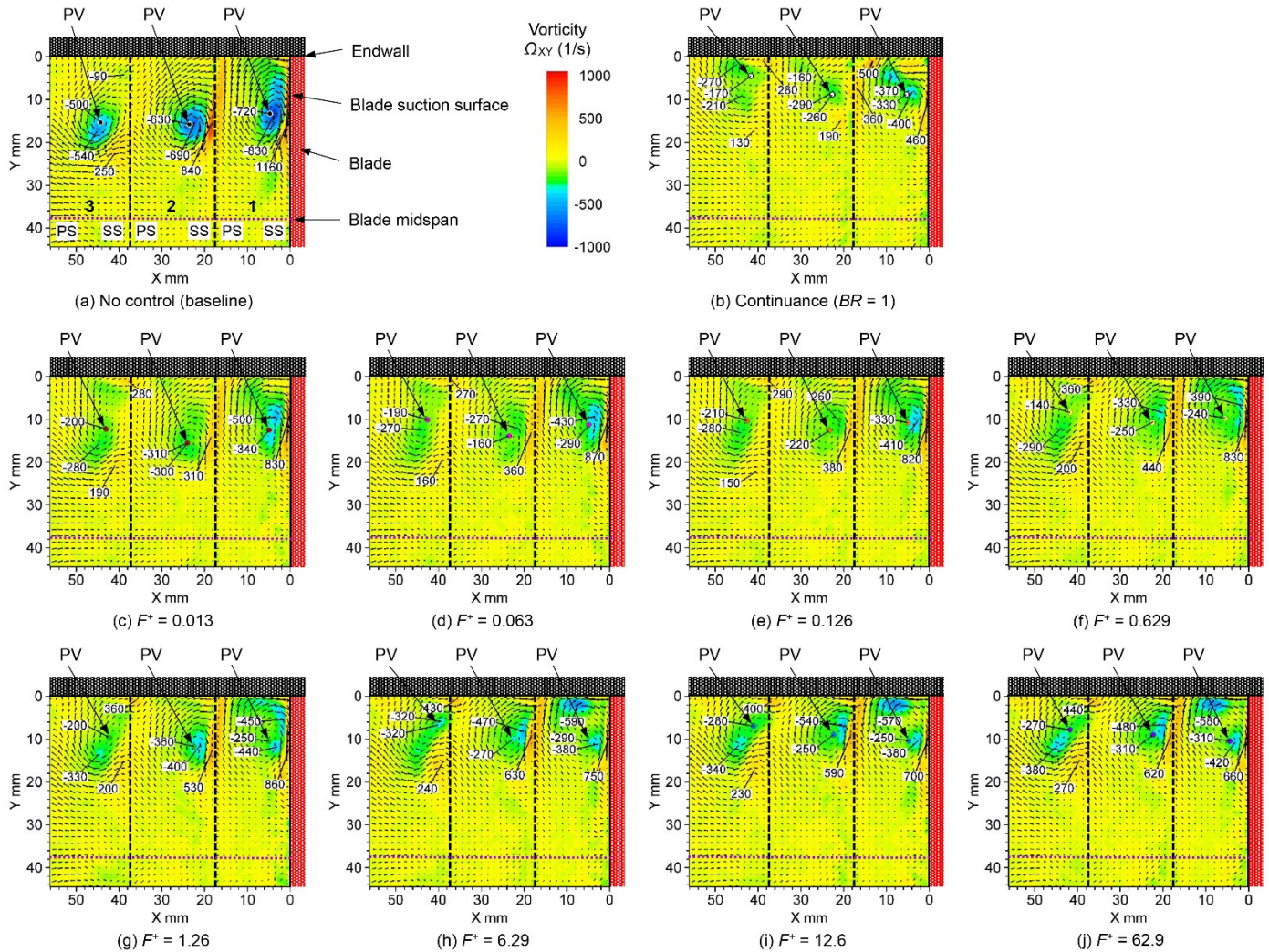


**Figure 26.** Vorticity distributions of secondary flow at the outlet of the linear turbine cascade at various burst frequencies ( $BR = 0.5$ ).

Figure 27 shows the change in the vortex at the center position of the passage vortex by changing the burst frequency from Figure 26. In passage 1, shown in Figure 27a, despite the burst ratio being halved ( $BR = 0.5$ ), the vorticity at the passage vortex center is approximately the same as the continuous flow control line ( $BR = 1$ ) at any burst frequency. At  $F^+ = 0.629$ , the vorticity decreased by as much as 67% compared with that at no control. A 54% decrease was observed for the magnitude of vorticity at  $F^+ = 0.629$  of  $BR = 0.5$  compared to that of the continuous flow control with  $BR = 1$  (54% decrease). This indicates that the burst flow control at  $BR = 0.5$  also has the same or a greater vorticity reduction effect compared to the continuous flow control at  $BR = 1$ . In passage 2, shown in Figure 27b, the vorticity of the passage vortex center at any burst frequency of  $BR = 0.5$  is also close to that at continuous flow control. At  $F^+ = 0.063$ , the vorticity decreased by as much as 75% compared with that at no control. In passage 3, shown in Figure 27c, the vorticity was close

to that of continuous flow control at the low burst frequency before  $F^+ = 1.26$ . At  $F^+ = 0.629$ , the vorticity decreased by 72% compared with that at no control. In contrast, the vorticity increased to  $F^+ = 6.29$  or higher. As observed in Figure 23c, the interaction between the passage vortex and the upper endwall surface becomes stronger when moving the center position of the passage vortex to the upper endwall side at a high burst frequency.

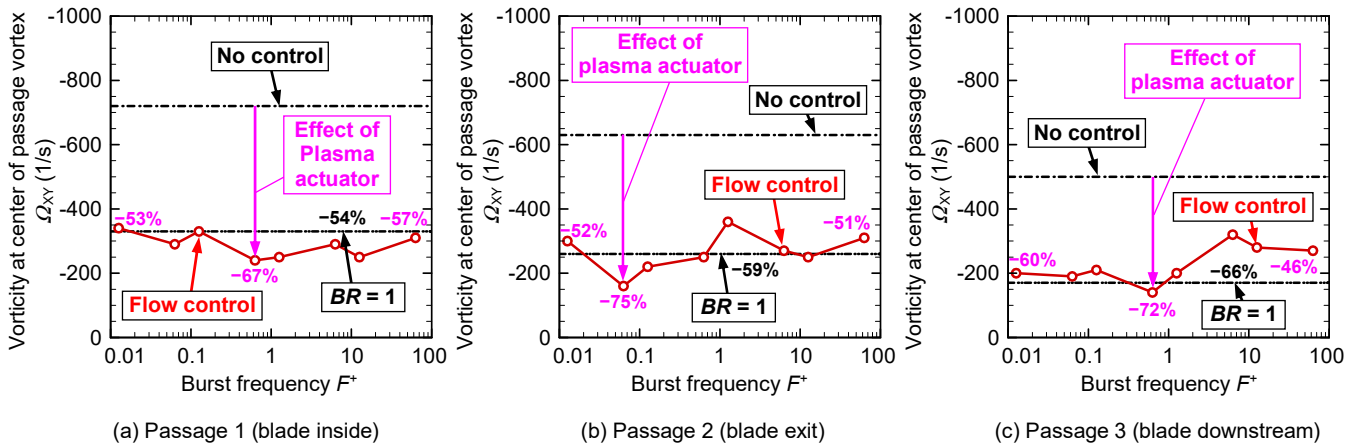


Figure 27. Vorticity at the center of passage vortex at various burst frequencies ( $BR = 0.5$ ).

Figure 28 illustrates the changes in the negative peak values of vorticity in response to changes in the burst frequency in the vorticity distribution shown in Figure 26. In passage 1, shown in Figure 28a, the negative peak vorticity is the lowest at  $F^+ = 0.629$ , and a decrease of 53% was observed compared with that at no control, which coincides with that at continuous flow control of  $BR = 1$ . As the burst frequency decreases, the negative peak value of the vorticity gradually increases. A 40% reduction in the magnitude of vorticity is observed at  $F^+ = 0.013$ . Conversely, when the burst frequency becomes larger than  $F^+ = 0.629$ , the magnitude of vorticity increases rapidly to  $F^+ = 6.29$  (where a 30% decrease in the magnitude of vorticity is observed), after which it remains approximately constant for values beyond  $F^+ = 6.29$ . In passage 2, as shown in Figure 28b, the negative vorticity is lowest at  $F^+ = 0.126$ , and a 62% decrease is observed compared with that at no control, which is marginally lower than that at continuous flow control of  $BR = 1$  (59% reduction). At lower burst frequencies lower than  $F^+ = 0.126$ , a slight increase in vorticity is observed (55% reduction at  $F^+ = 0.013$ ). In contrast, higher burst frequencies after  $F^+ = 0.126$  gradually increase the vorticity as the burst frequency becomes higher (22% reduction at  $F^+ = 12.6$ ). As seen in Figure 28c, when the burst frequency is lower than  $F^+ = 0.629$ , the vorticity is virtually constant, and a decrease in vorticity by up to 50% is observed at  $F^+ = 0.063$ . This is practically the same value as that at continuous flow control ( $BR = 1$ ). In contrast, at  $F^+$  values of 1.26 or higher, higher  $F^+$  values result in higher vorticity (30% reduction at  $F^+ = 62.9$ ). As observed in the vorticity distributions at a higher burst frequency in Figure 26g–j, the passage vortex moves to the upper endwall side, the interference between the vortex and the endwall surface becomes stronger, and a larger vorticity region is generated.

The results from Figures 19–28 are summarized as follows: low burst frequency values result in a decrease in the peak velocity of the passage vortex and passage vortex center and negative peak vorticities; however, the position of the passage vortex center and turbulence intensity at the vortex center increase. In contrast, a high burst frequency value leads to decrease in the position of the vortex center and turbulence intensity of the passage; however, an increase is observed in the peak velocity of the passage vortex, vorticity at the vortex center, and negative peak vorticity. The dimensionless burst frequency around  $F^+ = 1$  is balanced between the two effects, which appears to be appropriate.

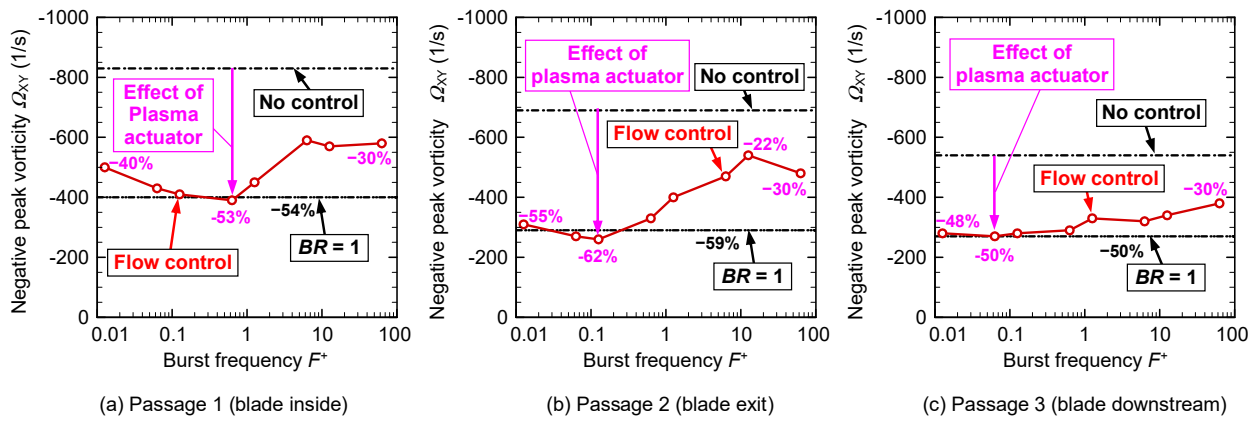


Figure 28. Negative peak vorticity at various burst frequencies ( $BR = 0.5$ ).

To consider and discuss the energy consumption in the burst mode operation,  $VRR$  and  $\eta_{burst}$  were also analyzed using Equations (6) and (7). The results of the analysis are shown in Figure 29. Figure 29a shows the vorticity at the center of the passage vortex in passage 1 at various burst frequencies, which is the same as in Figure 27a. The difference between the vorticities with no control and continuous flow control ( $BR = 1$ ) is defined as 1 (100%) in this figure. Figure 29b shows the vorticity reduction ratio calculated using Equation (4), as previously described. Despite  $BR = 0.5$ , the effect of the vorticity reduction ratio at various burst frequencies was greater than 1, which means that the reduction effect was larger than that at  $BR = 1$ . The maximum  $VRR$  is 1.23 (123%) at  $F^+ = 0.629$ . The maximum  $VRR$  is 0.97 (97%) at  $F^+ = 0.013$ . Figure 29c shows the burst efficiency of vorticity reduction at various burst frequencies. The efficiency considers the electric energy consumption at  $BR = 0.5$ , and the burst efficiency is twice that of the  $VRR$ , as shown in Figure 29b. The maximum efficiency is 2.46 (246%) at  $F^+ = 0.629$ , which is approximately 2.5 times higher than the efficiency at the baseline of the continuous mode operation,  $BR = 1$ . The variation owing to the burst frequency is gentle; however, the efficiency around  $F^+ = 1$  is considered the most suitable. At both lower and higher burst frequencies, away from  $F^+ = 1$ , the burst efficiency tends to decrease the vorticity reduction effect.

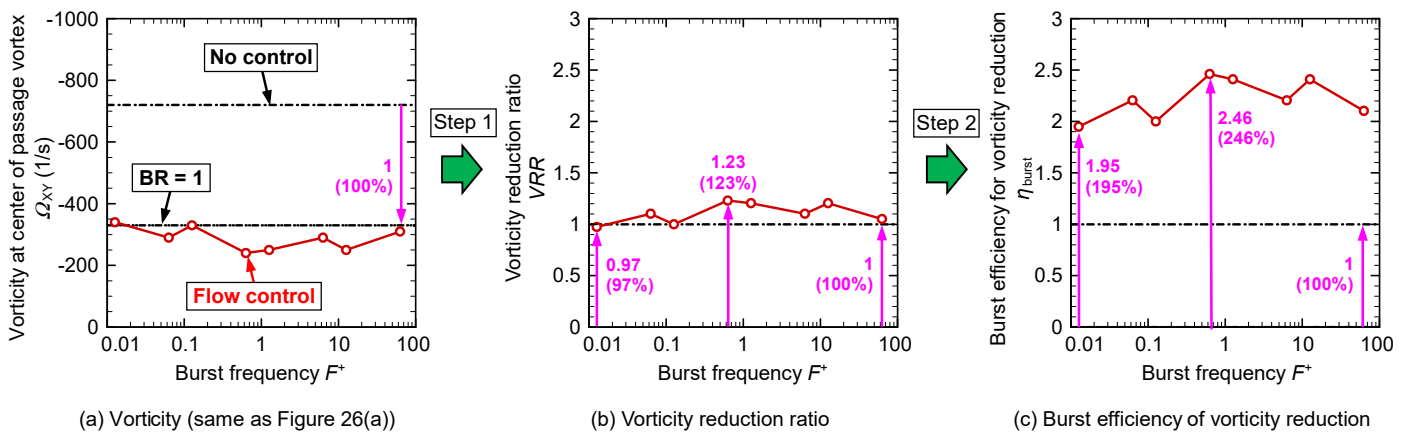


Figure 29. Burst efficiency analyzed by the vorticity at the center of passage vortex in passage 1 at various burst frequencies ( $BR = 0.5$ ).

Some studies regarding the flow separation control on the suction surface of single airfoils [4,5,11] concluded that the most effective non-dimensional burst frequency was around  $F^+ = 1$ . Although this study dealt with the passage vortex reduction of turbine blades, the results were similar to those of the flow separation reduction control of single airfoils.

#### 4. Concluding Remarks

An experiment was conducted using a DBD plasma actuator to reduce the passage vortex generated in a turbine cascade. This study focused on the drive in the burst mode of a plasma actuator and clarified how the flow field changes when the burst ratio and burst frequency are changed.

The main experimental results were as follows.

**Burst ratio.** The non-dimensionalized burst frequency was fixed at  $F^+ = 1.26$ , and the burst ratio was varied at  $BR = 0.01$  (1% operation) to 1 (100% operation, continuous mode).

- (1) Generally, as the burst ratio increases, the passage vortex weakens, and the center of the passage vortex moves more toward the upper endwall surface and blade suction surface side. However, it was clarified that the velocity distribution, streamlines of the secondary flow, turbulence intensity distribution, and vorticity distribution did not necessarily change proportionally with the change in the burst ratio and that the turbulence intensity and vorticity were decreased or increased temporarily by the movement of the passage vortex and the interaction between the passage vortex and the upper endwall surface.
- (2) The burst mode operation of the plasma actuator is more effective than continuous mode operation in terms of electric energy consumption. In particular, at a very low burst ratio of  $BR = 0.05$  (5% operation), the burst efficiency becomes as much as 11.54 (1154%) compared with that in continuous mode operation.

**Burst frequency.** The burst ratio was fixed at  $BR = 0.5$ , and the non-dimensional burst frequency varied from  $F^+ = 0.013$  to 62.9.

- (3) Regarding the burst frequency, when the burst frequency is low, the peak velocity of the passage vortex, vorticity at the passage vortex center, and negative peak vorticity decrease; however, the distance of the center of the passage vortex from the upper endwall surface and turbulence intensity at the vortex center increase. In contrast, when the burst frequency is high, the position of the vortex center and the turbulence intensity of the passage vortex center decrease, but the peak velocity of the passage vortex, vorticity at the vortex center, and negative peak vorticity increase. The non-dimensionalized burst frequency around  $F^+ = 1$  is balanced between the two effects, which seems to be appropriate.
- (4) When the energy consumption in burst mode operation is considered, the maximum efficiency is 2.46 (246%) at  $F^+ = 0.629$ , which is approximately 2.5 times higher than the efficiency at the baseline of continuous mode operation.

**Funding:** This research was funded by the Japan Society for the Promotion of Science (JSPS), Grants-in-Aid for Scientific Research (KAKENHI), Grant Number 21K03868.

**Institutional Review Board Statement:** Not applicable.

**Informed Consent Statement:** Not applicable.

**Data Availability Statement:** The data supporting the findings of this study are available from the corresponding author upon reasonable request.

**Acknowledgments:** The author would like to thank Takehiko Segawa of AIST for his support with the PIV experiments.

**Conflicts of Interest:** The author declares no conflict of interest regarding the publication of this article.

#### Nomenclature

$BR$	Burst ratio
$C$	Blade chord length (mm)
DBD	Dielectric barrier discharge
$f_{\text{base}}$	Base frequency (1/s)
$f_{\text{burst}}$	Burst frequency (1/s)
$F^+$	Non-dimensionalized burst frequency

$H$	Blade height (mm)
$L$	Spanwise width of electrodes of plasma actuator (mm)
$N$	Number of blades
PIV	Particle image velocimetry
PV	Passage vortex
Re	Reynolds number
$S$	Blade pitch (mm)
$T$	Time (s)
$t$	Thickness (mm)
$Tu$	Turbulence intensity (%)
$U$	Velocity (m/s)
$V$	Input voltage (kV)
VRR	Vorticity reduction ratio
$X$	Horizontal coordinate of PIV domain (mm)
$Y$	Vertical coordinate of PIV domain (mm)
$Z$	Axial coordinate of turbine cascade (mm)
<i>Greek symbols</i>	
$\alpha$	Blade angle ( $^{\circ}$ )
$\eta$	Efficiency
$\Omega$	Vorticity component (1/s)
$\zeta$	Blade stagger angle ( $^{\circ}$ )
<i>Subscripts</i>	
ax	Axial
burst	Burst mode operation
in	Inlet flow
FS	Freestream
out	Outlet flow
PA	Plasma actuator
p-p	Peak to peak
XY	X-Y measurement plane

## References

1. Corke, T.C.; Post, M.L.; Orlov, D.M. SDBD plasma enhanced aerodynamics: Concepts, optimization and applications. *Prog. Aerosp. Sci.* **2007**, *43*, 193–217. [[CrossRef](#)]
2. Corke, T.C.; Enloe, C.L.; Wilkinson, S.P. Dielectric barrier discharge plasma actuators for flow control. *Annu. Rev. Fluid Mech.* **2010**, *42*, 505–529. [[CrossRef](#)]
3. Wang, J.J.; Choi, K.S.; Feng, L.H.; Jukes, T.N.; Whalley, R.D. Recent developments in DBD plasma flow control. *Prog. Aerosp. Sci.* **2013**, *62*, 52–78. [[CrossRef](#)]
4. Corke, T.; Post, M. Overview of Plasma Flow Control: Concepts, Optimization, and Applications. In Proceedings of the 43rd AIAA Aerospace Sciences Meeting and Exhibit, Reno, NV, USA, 10–13 January 2005. [[CrossRef](#)]
5. Benard, N.; Jolibois, J.; Moreau, E. Lift and drag performances of an axisymmetric airfoil controlled by plasma actuator. *J. Electrostat.* **2009**, *67*, 133–139. [[CrossRef](#)]
6. Lombardi, A.; Bowles, P.; Corke, T. Closed-Loop Dynamic Stall Control Using a Plasma Actuator. In Proceedings of the 50th AIAA Aerospace Sciences Meeting including the New Horizons Forum and Aerospace Exposition, Nashville, TN, USA, 9–12 January 2012. [[CrossRef](#)]
7. Asada, K.; Fujii, K. Burst Frequency Effect of DBD Plasma Actuator on the Control of Separated Flow over an Airfoil. In Proceedings of the 6th AIAA Flow Control Conference, New Orleans, LA, USA, 25–28 June 2012. [[CrossRef](#)]
8. Sekimoto, S.; Nonomura, T.; Fujii, K. Burst-Mode Frequency Effects of Dielectric Barrier Discharge Plasma Actuator for Separation Control. *AIAA J.* **2017**, *55*, 1385–1392. [[CrossRef](#)]
9. Abdollahzadeh, M.; Pascoa, J.; Oliveira, P. Comparison of DBD plasma actuators flow control authority in different modes of actuation. *Aerosp. Sci. Technol.* **2018**, *78*, 183–196. [[CrossRef](#)]
10. Wang, L.; Wong, C.W.; Alam, M.; Zhou, Y. Post-stall flow control using a sawtooth plasma actuator in burst mode. *Aerosp. Sci. Technol.* **2020**, *107*, 106251. [[CrossRef](#)]
11. Okada, K.; Asada, K.; Aono, H.; Nonomura, T.; Fujii, K. Unified mechanisms for separation control around airfoil using plasma actuator with burst actuation over Reynolds number range of  $10^3$ – $10^6$ . *Phys. Fluids* **2020**, *32*, 025102. [[CrossRef](#)]

12. Ogawa, T.; Asada, K.; Sekimoto, S.; Tatsukawa, T.; Fujii, K. Dynamic Burst Actuation to Enhance the Flow Control Authority of Plasma Actuators. *Aerospace* **2021**, *8*, 396. [[CrossRef](#)]
13. Koide, Y.; Sasaki, R.; Kameya, Y.; Motosuke, M. A burst wave-induced plasma actuator for controlling separated flow over a backward-facing step at low Reynolds numbers. *Exp. Therm. Fluid Sci.* **2015**, *66*, 72–78. [[CrossRef](#)]
14. Li, Y.-H.; Wu, Y.; Zhou, M.; Su, C.-B.; Zhang, X.-W.; Zhu, J.-Q. Control of the corner separation in a compressor cascade by steady and unsteady plasma aerodynamic actuation. *Exp. Fluids* **2010**, *48*, 1015–1023. [[CrossRef](#)]
15. Saddoughi, S.; Bennett, G.; Boespflug, M.; Puterbaugh, S.L.; Wadia, A.R. Experimental investigation of tip clearance flow in a transonic compressor with and without plasma actuators. *ASME J. Turbomach.* **2015**, *137*, 041008. [[CrossRef](#)]
16. Huang, J.; Corke, T.C.; Thomas, F.O. Unsteady Plasma Actuators for Separation Control of Low-Pressure Turbine Blades. *AIAA J.* **2006**, *44*, 1477–1487. [[CrossRef](#)]
17. Rizzetta, D.; Visbal, M. Numerical Investigation of Plasma-Based Flow Control for a Transitional Highly-Loaded Low-Pressure Turbine. In Proceedings of the 45th AIAA Aerospace Sciences Meeting and Exhibit, Reno, NV, USA, 8–11 January 2007. [[CrossRef](#)]
18. De Giorgi, M.G.; Ficarella, A.; Marra, F.; Pescini, E. Micro DBD plasma actuators for flow separation control on a low pressure turbine at high altitude flight operating conditions of aircraft engines. *Appl. Therm. Eng.* **2017**, *114*, 511–522. [[CrossRef](#)]
19. Pescini, E.; Marra, F.; De Giorgi, M.G.; Francioso, L.; Ficarella, A. Investigations of the actuation effect of a single DBD plasma actuator for flow separation control under simulated low-pressure turbine blade conditions. In Proceedings of the ASME Turbo Expo 2016: Turbomachinery Technical Conference and Exposition. Volume 2B: Turbomachinery, Seoul, Korea, 13–17 June 2016. [[CrossRef](#)]
20. Sieverding, C.H. Recent progress in the understanding of basic aspects of secondary flows in turbine blade passages. *ASME J. Eng. Gas Turbines Power* **1985**, *107*, 248–257. [[CrossRef](#)]
21. Stephens, J.E.; Corke, T.; Morris, S.C. Blade-Mounted Single Dielectric Barrier Discharge Plasma Actuators in a Turbine Cascade. *J. Propuls. Power* **2011**, *27*, 692–699. [[CrossRef](#)]
22. Van Ness, D.K.; Corke, T.C.; Morris, S.C. Plasma Actuator Blade Tip Clearance Flow Control in a Linear Turbine Cascade. *J. Propuls. Power* **2012**, *28*, 504–516. [[CrossRef](#)]
23. Wang, Z.; Yu, J.; Chen, F.; Song, Y. Effect of multiple DBD plasma actuators on the tip leakage flow structure and loss of a turbine cascade. *Int. J. Heat Fluid Flow* **2019**, *77*, 377–387. [[CrossRef](#)]
24. Yu, J.; Yu, J.; Chen, F.; Wang, C. Numerical study of tip leakage flow control in turbine cascades using the DBD plasma model improved by the parameter identification method. *Aerosp. Sci. Technol.* **2018**, *84*, 856–864. [[CrossRef](#)]
25. Yu, J.; Wang, Z.; Chen, F.; Yu, J.; Wang, C. Kriging surrogate model applied in the mechanism study of tip leakage flow control in turbine cascade by multiple DBD plasma actuators. *Aerosp. Sci. Technol.* **2018**, *85*, 216–228. [[CrossRef](#)]
26. Yu, J.; Lu, Y.; Wang, Y.; Chen, F.; Song, Y. Experimental study on the plasma actuators for the tip leakage flow control in a turbine cascade. *Aerosp. Sci. Technol.* **2021**, *121*, 107195. [[CrossRef](#)]
27. Matsunuma, T. Effects of the Installation Location of a Dielectric Barrier Discharge Plasma Actuator on the Active Passage Vortex Control of a Turbine Cascade at Low Reynolds Numbers. *Actuators* **2022**, *11*, 129. [[CrossRef](#)]
28. Matsunuma, T. Unsteady flow field of an axial-flow turbine rotor at a low Reynolds number. *Trans. ASME J. Turbomach.* **2007**, *129*, 360–371. [[CrossRef](#)]
29. Kriegseis, J.; Möller, B.; Grundmann, S.; Tropea, C. Capacitance and power consumption quantification of dielectric barrier discharge (DBD) plasma actuators. *J. Electrostat.* **2011**, *69*, 302–312. [[CrossRef](#)]
30. Ashpis, D.E.; Laun, M.C.; Griebeler, E.L. Progress toward accurate measurements of power consumptions of DBD plasma actuators. In Proceedings of the 50th AIAA Aerospace Sciences Meeting including the New Horizons Forum and Aerospace Exposition, Nashville, TN, USA, 9–12 January 2012. [[CrossRef](#)]
31. Benard, N.; Moreau, E. Electrical and mechanical characteristics of surface AC dielectric barrier discharge plasma actuators applied to airflow control. *Exp. Fluids* **2014**, *55*, 1–43. [[CrossRef](#)]